



## **Abstract**

This study employs the Coupled-Ocean-Atmosphere-Wave-Sediment-Transport (COAWST) modeling system to quantitatively assess the seasonal suspension, transport, and annual fate of Pearl River-derived sediment (riverine slow-settling single fine grains and high-settling flocs) on the northern continental shelf of the South China Sea (SCS). Following careful model validation, a series of sensitivity experiments were conducted to investigate the effects of tides, waves, background circulation, sediment settling velocity, critical shear stress, and sediment spin-up durations. The results reveal strong seasonal variations in sediment dynamics driven by the East Asian monsoon. During the wet summer, weaker hydrodynamic conditions promote the initial deposition of riverine sediment via the surface buoyant plume. In contrast, stronger winds and waves during winter enhance sediment resuspension and southwestward transport, particularly toward the Beibu Gulf. Spatially, approximately two-thirds of the annual Pearl River-derived sediment load is retained near the estuary. About 9% reaches the continental shelf east of the PRE, while similar proportions accumulate in the Beibu Gulf and south of Hainan Island. Sensitivity experiments highlight the distinct roles of different physical forcings: tidal dynamics strongly influence sediment behavior in the estuary, where the absence of tidal forcing reduces bottom shear stress, leading to increased local deposition and reduced offshore transport. Wave forcing plays a dominant role in sediment resuspension near the river mouth and along the coast, especially during winter. Excluding waves leads to greater sediment retention near the estuary and diminished



transport toward distant regions. Ambient circulation, particularly in summer, is essential for eastward sediment transport; when it is omitted, northeastward dispersal is greatly diminished. Model outcomes are also sensitive to sediment parameterization. Using non-seasonal critical shear stress for erosion increases wintertime sediment mobility east of the Leizhou Peninsula. Higher settling velocities decrease suspended sediment concentrations and promote near-source retention, limiting long-distance transport. Spin-up duration experiments indicate that Pearl River-derived sediment, which enters and accumulates in various regions of the model domain during the first year, continues to migrate southwestward in the second year under the influence of the mean annual flow field. In contrast, the spin-up duration of seabed sediment has little impact on the retentions of Pearl River-derived sediment on the shelf. Overall, this study reveals the transport pathway and fate of the Pearl River-derived sediment and provides a model-based assessment of its seasonal behavior and dispersal mechanisms on the northern SCS shelf. It identifies key physical drivers regulating sediment transport and deposition patterns, offering new insight into sediment fate in a monsoon-dominated shelf system.

## **Keywords**

Riverine sediment transport; Sediment retention; Numerical modeling; Pearl River Estuary

## **1. Introduction**

The transport process of suspended sediment from river source to ocean sink is an important link in the global material cycle ([Geyer et al., 2004](#); [McKee et al., 2004](#);

54 [Kuehl et al., 2016](#); [Liu et al., 2016](#); [Cao et al., 2019](#)). Much of the riverine sediment is  
55 trapped on the shallow shoals in estuaries, while the rest is transported by buoyant  
56 plume out of the estuary ([Meade, 1969](#); [Burchard et al., 2018](#); [Zhang et al., 2019](#)). The  
57 riverine sediment carried by the buoyant plume has a significant impact on the water  
58 quality, ecology, and geomorphology of the estuaries and continental shelves ([Wright](#)  
59 [and Coleman, 1973](#); [Turner and Millward, 2002](#)).

60       The transport and deposition of riverine sediments from river source to estuarine,  
61 coastal, and shelf environments are controlled by diverse physical processes,  
62 including tidal forces, wave action, and shelf circulation dynamics ([Dalyander et al.,](#)  
63 [2013](#); [Gao and Collins, 2014](#); [Xu et al., 2016](#); [Warner et al., 2017](#); [Zang et al., 2019](#);  
64 [Wang et al., 2020](#)). Tides play a critical role in sediment transport dynamics in  
65 estuarine and shelf regions, as spring tides typically produce higher bed shear stress,  
66 enhanced sediment resuspension, and greater offshore sediment transport flux  
67 compared to neap tides ([Bever and MacWilliams, 2013](#); [Zhang et al., 2019](#); [Wang et](#)  
68 [al., 2020](#)). In nearshore regions, wave-induced bed shear stress often exceeds  
69 current-induced stress by an order of magnitude ([Xue et al., 2012](#); [Dalyander et al.,](#)  
70 [2013](#)). Furthermore, wave-driven sediment resuspension frequently surpasses, and is  
71 often several times greater than, the peak levels achieved by current-induced  
72 resuspension ([Sanford, 1994](#); [Harris et al., 2008](#); [Brand et al., 2010](#); [Xu et al., 2016](#)).  
73 In shelf regions, circulation patterns significantly modulate sediment transport, with  
74 the magnitude of along-shelf transport substantially exceeding the cross-shelf  
75 component in most areas ([Nittrouer and Wright, 1994](#); [Geyer et al., 2004](#); [Gao and](#)

[Collins, 2014](#); [Wang et al., 2020](#)).

Furthermore, sediment properties, including settling velocity ([Xia et al., 2004](#); [Chen et al., 2010](#); [Cheng et al., 2013](#)), critical shear stress for erosion ([Dong et al., 2020](#)), and bed grain size distribution ([Xue et al., 2012](#); [Bever and MacWilliams, 2013](#)), significantly influence sediment transport dynamics and deposition/resuspension processes. Settling velocity can influence the location of sediment depocenters, with higher settling velocities leading to more proximal entrapment and vice versa ([Ralston and Geyer, 2017](#)). Similarly, critical shear stress for erosion can affect the resuspension of deposited sediment, with higher critical shear stress resulting in less resuspension and more deposition especially during neap tides and weak wind wave periods ([Dong et al., 2020](#); [Choi et al., 2023](#)).

A comprehensive understanding of sediment transport and deposition from river source to ocean sink requires the integrated consideration of both physical forcing factors and inherent sediment characteristics. Here, we present the transport and deposition of the Pearl River-derived sediments on the continental shelf as a case study. The Pearl River, ranking as China's second-largest river in terms of freshwater discharge ([Hu et al., 2011](#)), forms the Pearl River Estuary (PRE) in its lower reaches (Figures 1 and S1). Its freshwater and sediment discharge are primarily delivered through eight major outlets (Figure S1b; [Wu et al., 2016](#); [Zhang et al., 2019](#); [Zhang et al., 2025](#)), forming distinct buoyant plumes that extend across the northern South China Sea (SCS) shelf ([Zhang et al., 2025](#)). The present average annual (2001-2022) freshwater and riverine sediment loads are  $2.74 \times 10^{11} \text{ m}^3$  and  $2.84 \times 10^7$  tons,

respectively, as reported by the Ministry of Water Resources of the People's Republic of China (<http://www.mwr.gov.cn/sj/#tjgb>). The distribution of these inputs shows significant seasonal variability: approximately 80% of the freshwater and 95% of the sediment load are transported during the wet summer season (April to September), while the remaining portion is discharged during the dry winter season (Xia et al., 2004).

The northern SCS, shaped by the East Asian Monsoon, displays marked seasonal contrasts, featuring winter monsoon winds averaging  $7\text{--}10\text{ m s}^{-1}$  and summer winds typically below  $6\text{ m s}^{-1}$  (Su, 2004; Ou et al., 2009). This seasonal shift drives coastal currents: northeastward in summer and southwestward in winter (Gan et al., 2009; Gan et al., 2013). Beyond the coastal zone, the consistent SCS Warm Current (SCSWC) flows northeastward along the shelf break and inner continental slope toward the Taiwan Strait, originating near Hainan Island and persisting year-round, even during the winter northeast monsoon, across a remarkable distance of 600–700 km to the southern tip of the Taiwan Strait (Su, 2004; Yang et al., 2008).

The PRE is situated in the central part of the northern South China Sea boundary, positioned between the Taiwan Banks and Hainan Island. The PRE has a micro-tidal and mixed semi-diurnal regime, with daily inequality in the range and in the time between the high and low tides (Mao et al., 2004). The neap and spring tides alternately influence the water elevation downstream of the estuary, with tidal ranges varying from approximately 0.7 m during neap tides to over 2 m during spring tides (Chen et al., 2016; Gong et al., 2018b). The PRE and the nearby shelf exhibit strong

seasonal variation in water column stability and are highly stratified during the wet summer season, while the PRE becomes partially mixed or vertically well-mixed during the dry winter season ([Dong et al., 2004](#)). Offshore of the PRE region, wave conditions display distinct seasonal patterns: the waves are mild during summer, and become stronger during winter, marked by larger southeasterly waves ([Gong et al., 2018a](#); [Gong et al., 2018b](#); [Zhang et al., 2021](#)).

Previous studies have focused on sediment transport within the PRE ([Zhang et al., 2019](#); [Zhang et al., 2021](#); [Ma et al., 2024](#)). Most Pearl River-derived sediments are deposited within the estuary, and neglecting tidal effects can lead to higher deposition rates and lower offshore sediment flux when compared to those with tides ([Hu et al., 2011](#)). The depositional dynamics of sediments from different PRE outlets are regulated by outlet location, topography, and tidal conditions, with neap tides favoring sediment accumulation on shoals and spring tides driving erosion and enhancing offshore sediment transport ([Zhang et al., 2019](#)). Waves further intensify both lateral trapping within the PRE and offshore sediment transport ([Liu and Cai, 2019](#); [Zhang et al., 2021](#)).

However, numerical studies on the transport of the Pearl River-derived sediments across the continental shelf remain scarce, even amidst the widespread adoption of computer modeling approaches. Previous research on the distribution of these sediments has primarily relied on analyses of seismic profiles, gravity cores, and laboratory-based radiometric dating of sediment samples ([Ge et al., 2014](#); [Liu et al., 2014](#); [Cao et al., 2019](#); [Lin et al., 2020](#); [Chen et al., 2023](#)). Outside the PRE, gravity

core and seismic survey data were used to examine the Holocene sedimentary processes, revealing two distinct mud depo-centers: an eastward proximal depo-center extending southeastward from the PRE's mouth and a southwestward distal mud belt ([Ge et al., 2014](#); [Liu et al., 2014](#); [Chen et al., 2023](#)). However, seismic and drilling data cannot confirm that the Pearl River sediment can be transported to the Beibu Gulf ([Ge et al., 2014](#)). Due to the lack of sufficient gravity core samples and seismic data, it is difficult to quantitatively attribute the sediment in the Beibu Gulf to the Pearl River-derived sediment ([Cao et al., 2019](#)). Afterward, [Lin et al. \(2020\)](#) used the  $^{226}\text{Ra}$ — $^{238}\text{U}$  and  $^{232}\text{Th}$ — $^{238}\text{U}$  endmembers model based on measurements of radionuclides in the surface sediment samples. They found that approximately 15% of the surface sediment in the nearshore area of the Beibu Gulf originates from the PRE region. However, their studies only address the proportion of the PRE sediment in the surface sediment of the Beibu Gulf, without directly indicating the seasonal transport pathways, flux, and annual deposition of the sediment from the Pearl River.

A gap persists in understanding how physical processes (such as tides, waves, and ambient circulations) and sediment characteristics (such as critical shear stress for erosion, settling velocity) and sediment initial conditions influence the seasonal suspension, transport, and annual deposition of the Pearl River-derived sediment on the shelf. Specifically, this study focuses on sediment classes 4 and 5 in Table 1, which represent the Pearl River-derived components: slow-settling single fine grains (Class 4) and fast-settling flocs (Class 5), in contrast to the background seabed sediments represented by classes 1 to 3. To address this, we utilize numerical

modeling, complemented by extensive collection of field observations and seabed grain size distribution data for model calibration and validation—a highly effective approach for exploring mechanisms and testing hypotheses derived from limited observational datasets. This study aims to systematically investigate the dispersal dynamics of the Pearl River-derived sediment over the northern South China Sea shelf, with particular emphasis on the following objectives:

(1) Quantify the seasonal dispersal and annual deposition of the Pearl River-derived sediment (classes 4 and 5 in Table 1) over the continental shelf.

(2) Examine the relative roles of physical forcings (tides, waves, and ambient circulations), sediment characteristics (critical shear stress for erosion, settling velocity) and (Pearl River-derived versus Seabed) sediment spin-up durations on the dispersal of the Pearl River-derived sediment.

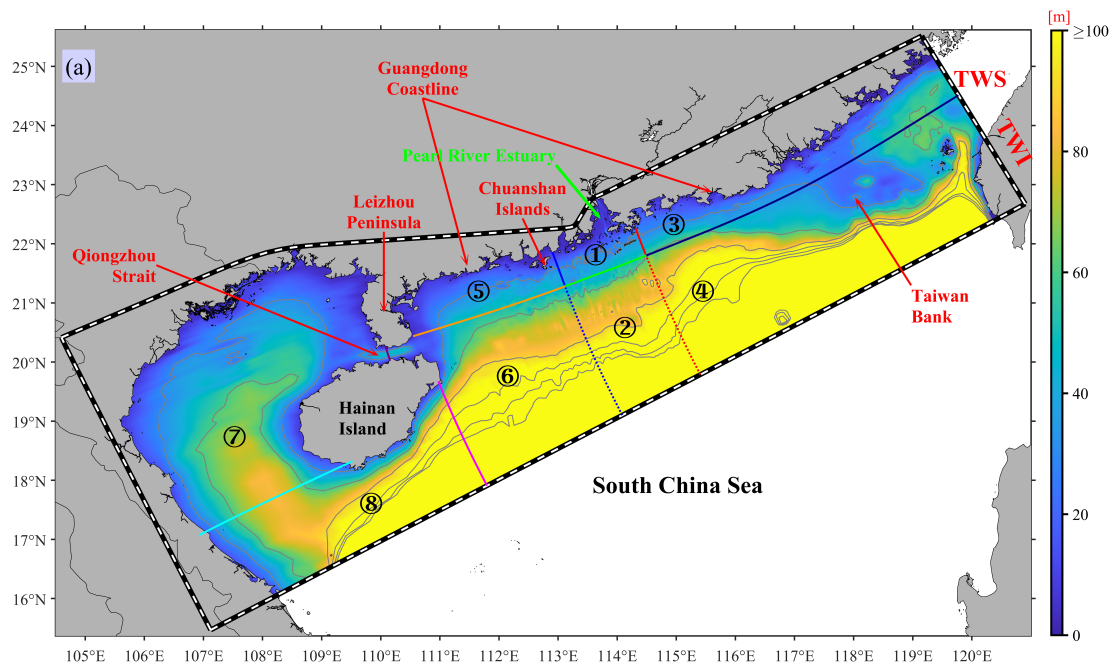


**Figure 1.** Bathymetry (shading) and isobath contours of the study area, with the ROMS/SWAN model grid domain outlined by black-to-white dashed lines. Circled numbers ① - ⑧ denote the eight regions: "Proximal", "Southern", "Eastern", "Southeastern", "Western", "Southwestern", "Gulf", and "Distal" regions, as defined by transects and detailed in Section 2.1. The abbreviations TWI and TWS mean Taiwan Island and Taiwan Strait, respectively. The gray contours represent 30-180 m isobaths at 30 m intervals, a consistent feature maintained in all subsequent figures that include these isobath contours.

## 2. Methods

### 2.1 Model coupling

This study employed the Coupled Ocean Atmosphere Wave Sediment Transport (COAWST, version 3.4) modeling system ([Warner et al., 2005](#); [Warner et al., 2008](#); [Warner et al., 2010](#)), which includes a Model Coupling Toolkit (MCT) to facilitate data exchange among different modules ([Jacob et al., 2005](#); [Larson et al., 2005](#)). The COAWST system consists of several modeling components, mainly comprises a hydrodynamic module (Regional Ocean Modeling System; ROMS) ([Shchepetkin and McWilliams, 2005](#); [Haidvogel et al., 2008](#)), an atmospheric module (Advanced Research Weather Research and Forecasting; WRF) ([Skamarock et al., 2005](#)), a wave module (Simulating Waves Nearshore; SWAN) ([Booij et al., 1999](#)), and a sediment transport module (Community Sediment Transport Modeling System; CSTM) ([Warner et al., 2008](#)).



In this study, we established a coupling between ROMS, SWAN, and CSTM. The model grid covered the northern continental shelf of the South China Sea, including the PRE (Figure 1). The regional model was configured with  $170 \times 482$  horizontal grid cells, with horizontal resolution varying from approximately 0.1 km near the PRE to about 10 km at outer open boundaries ([Hu et al., 2024](#); [Zhang et al., 2025](#)). The model grid bathymetry data was obtained from nautical charts compiled by the China Maritime Safety Administration and the General Bathymetric Chart of the Oceans (GEBCO) ([Weatherall et al., 2015](#)). The vertical grid used a terrain-following S-coordinate system ([Song and Haidvogel, 1994](#)) with 20 layers and a stretching transformation for higher resolution near the surface and bottom. For model validations, please refer to the Supplementary Material (Supplement Figures S1-S10).

To improve the understanding of the spatial-temporal variabilities in the riverine sediment dispersal, and the estimation of the fate of the Pearl River sediment during the wet summer season, dry winter season, and throughout the year, we partitioned the model domain into eight distinct regions delineated by various transects as illustrated in Figure 1. The division criteria are mainly based on the distance from the estuary and the natural separation by the Leizhou Peninsula and Hainan Island (Figure 1).

These regions include:

- ① Proximal region: Proximity to the estuary,
- ② Southern region: Located deeper in the southern part of the estuary,
- ③ Eastern region: Eastern side of the estuary, closer to the shoreline,
- ④ Southeastern region: Further offshore on the eastern side of the estuary,

⑤ Western region: Western side of the estuary, closer to the shoreline,

⑥ Southwestern region: Offshore on the western side of the estuary,

⑦ Gulf region: Mainly the Beibu Gulf,

⑧ Distal region: South of the Hainan Island.

By dividing the model domain into these delineated regions, we calculated the riverine sediment flux for each transect, thereby determining the total riverine sediment volume retained in each region.

## 2.2 ROMS model setup

For the ROMS model, we utilized the Generic Length Scale turbulence closure scheme ([Warner et al., 2005](#)) for vertical turbulence parameterization. The method of [Smagorinsky \(1963\)](#) was employed to calculate the horizontal eddy viscosity and diffusivity. The Flather and Chapman boundary conditions were applied to barotropic current and water elevation at open boundaries, respectively ([Flather, 1976](#); [Chapman, 1985](#)). Meanwhile, the open-boundary conditions for temperature, salinity, and sediment concentration were imposed by radiation methods ([Orlanski, 1976](#); [Raymond and Kuo, 1984](#)). Surface forcing (including wind, net shortwave radiation, air temperature, atmospheric pressure, specific/relative humidity, and rain, etc.) data were sourced from the Climate Forecast System Reanalysis of the National Centers for Environmental Prediction (NCEP) ([Saha et al., 2014](#)), with a temporal resolution of 1 h and a spatial resolution of  $0.3^\circ \times 0.3^\circ$ . Water level and current open-boundary conditions comprised two components: tidal and subtidal. The tidal component was obtained from the Oregon State University Tidal Prediction Software database ([Egbert](#)

[and Erofeeva, 2002](#)), while the subtidal component was interpolated from the HYbrid Coordinate Ocean Model (HYCOM) outputs ([Chassignet et al., 2007](#)).

## **2.3 Wave model setup**

The SWAN model was executed and coupled to the same grid as the ROMS model ([Warner et al., 2010](#)). It was driven by surface atmospheric forces, real-time water level, and current fields from the ROMS and boundary reanalysis data. Wave boundary conditions were specified using nonstationary wave parameters from outputs of the NOAA WAVEWATCH III global ocean wave model solutions ([Tolman et al., 2016](#)). Information was exchanged at 15-minute intervals to introduce wave-current interaction (WCI) between the ROMS and SWAN models ([McWilliams et al., 2004](#); [Kumar et al., 2012](#)). This exchange included significant wave height ( $H_{sig}$ ), surface peak wave period, mean wave direction and length, wave energy dissipation, and the percentage of breaking waves from SWAN to ROMS, as well as water level and current from ROMS to SWAN.

Additionally, the wave-current bottom boundary module based on [Madsen \(1994\)](#), was activated to simulate the wave-current bottom boundary layer. The vortex force module of wave forces was also activated to compute the wave-induced momentum flux, utilizing the method proposed by [McWilliams et al. \(2004\)](#) and implemented in COAWST by [Kumar et al. \(2012\)](#). The bottom friction was computed based on a logarithmic velocity profile ([Warner et al., 2008](#)).

## **2.4 Specifications of riverine input and sediment model**

The freshwater discharge for the Pearl River was specified at the northern

boundary using daily measured data from the Pearl River Water Resources Commission, while downstream precipitation within the Pearl River Basin was neglected. The full simulation model was initialized on the first day of January 2016 using temperature, salinity, and current fields interpolated from the HYCOM model, and it concluded on March 31, 2018. This study primarily analyzes the last 12 months, specifically from April 1, 2017, to March 31, 2018. This year was selected because the freshwater discharge and sediment load of the Pearl River closely approximated the average values of the past two decades, with a runoff of  $3.35 \times 10^{11} \text{ m}^3$  and a sediment load of  $3.45 \times 10^7$  tons, closely resembling the averages from 2001 to 2022.

Since the daily riverine sediment loads were unavailable, we modified the previous research results on sediment rating curves ([Zhang et al., 2012](#)) to suit for our study, as expressed by

$$y = 0.00002263x^{1.792} \quad (1)$$

where  $y$  is the Pearl River-derived suspended sediment concentration ( $\text{mg L}^{-1}$ ),  $x$  is the Pearl River freshwater discharge rate ( $\text{m}^3 \text{ s}^{-1}$ ). Based on this relationship, the total amount of Pearl River sediment input over our 12-months study period (Figure 3b) was 34.52 million tons, aligning closely with the annual load reported in 2017 by the Pearl River Water Resources Commission. The riverine sediment input, derived from the river discharge, was allocated across the eight outlets along the north boundary (Figure S1b) based on the distribution approach of [Hu et al. \(2011\)](#). The subsequent step involved establishing the proportion of seabed sediment particle size components. Sediments are typically categorized into three grain-size classes: clay ( $0\text{--}4 \text{ }\mu\text{m}$ ), silt

(4-63  $\mu\text{m}$ ), and sand (63-2000  $\mu\text{m}$ ), as outlined by [Shepard \(1954\)](#). Data on sediment particle size composition for the northern continental shelf of the South China Sea and the PRE area were acquired through multiple voyage observations ([Zhang et al., 2013](#); [Zhang et al., 2019](#)). Furthermore, publicly available data from published literature were compiled ([Gao et al., 2007](#); [Kirby et al., 2008](#); [Gao et al., 2010](#); [Huang et al., 2013](#); [Liu et al., 2014](#); [Wang et al., 2014](#); [Wang et al., 2015](#); [Wang et al., 2016](#); [Ge et al., 2017](#); [Lu et al., 2017](#); [Zhong et al., 2017](#); [Yang et al., 2018](#); [Ge et al., 2019](#)). Finally, component distribution data for different particle size classes of seabed sediment were obtained from a total of 1981 measured stations (Figure 2a-c).

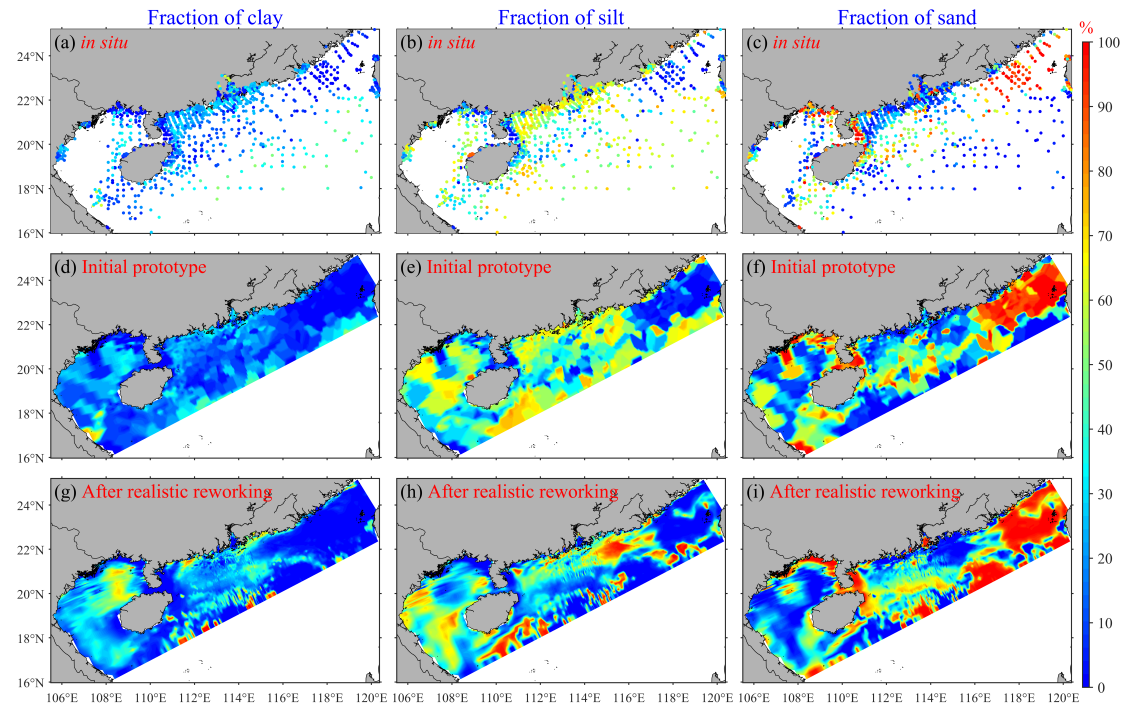


**Figure 2.** Row 1 presents the spatial distribution patterns of seabed sediment fractions derived from 1981 sampling sites, while Row 2 demonstrates the initial spatial distribution prototype of seabed sediment fractions developed based on the

302 observational data presented in Row 1. Row 3 shows the spatial distribution patterns  
303 of seabed sediment fractions following the completion of spin-up phase in the Control  
304 run case on April 1st, 2017, with Columns 1, 2, and 3 representing the fractions of  
305 clay, silt, and sand, respectively.

306  
307 As illustrated in Figure 2a-c, the measured stations exhibit a widespread  
308 distribution, offering comprehensive coverage of the entire northern continental shelf  
309 of the South China Sea, including the PRE. Particularly dense distribution is observed  
310 in the PRE and the coastal areas of western Guangdong. These regions represent the  
311 primary scope of transport and deposition associated with the Pearl River-derived  
312 sediment. Hence, the stations utilized in this study well represent the distribution of  
313 bed sediment particle size components in these study areas. It is evident that among  
314 the stations in the offshore area of the northern continental shelf of the South China  
315 Sea, silt dominates, followed by clay, while sand with the largest particle size is the  
316 least abundant. This suggests a significant presence of terrestrial sediment or Pearl  
317 River sediment in the offshore area of the northern continental shelf of the South  
318 China Sea. It should be noted that the lack of in situ grain size distribution data in  
319 specific regions of the model domain, especially in the Beibu Gulf area, may lead to  
320 uncertainties in sediment transport predictions. We will address these limitations and  
321 quantify their potential errors in the discussion part of this study.

322 To derive the component proportions of the initial prototype field on the model  
323 grid, this study employed the Kriging method ([Krige, 1951](#)), widely recognized for

spatially interpolating various types of observational data. The sediment distribution pattern obtained through interpolation (Figure 2d-f) closely resembles the original 1981 measured sediment particle size distribution patterns (Figure 2a-c), suggesting the suitability of this interpolation method for the study area.

The initial prototype field underwent a 15-month spin-up period (from January 1, 2016, to March 31, 2017), during which the bottom sediment composition evolved under realistic hydrodynamic forcings from the ROMS, SWAN, and CSTM models. This method has been utilized in numerous previous studies, including those by [Bever et al. \(2009\)](#), [van der Wegen et al. \(2010\)](#), and [Zhang et al. \(2021\)](#). This process allows the initially idealized sediment distribution to evolve under realistic dynamic forcings, including tides, waves, and currents, thereby minimizing unreasonable spatial patterns introduced by the Kriging interpolation method. Such unreasonable spatial patterns may arise due to limitations in the number, representativeness, and timing of field sediment samples relative to the model start date. As a result, the sediment field after the spin-up period (Figures 2g-i) exhibits spatial patterns that are more physically plausible and better aligned with the hydrodynamic conditions of the study region. During both the 15-month spin-up period and the subsequent 12-month formal model experiments (see Section 2.6 and Table 2), the CSTM utilized five sediment classes (Table 1), representing a range of sediment sizes and characteristics. These included three types of seabed sediments (clay, silt, and sand, corresponding to sediment Classes 1 to 3 in Table 1) and two types of Pearl River-derived sediments (Class 4 and Class 5 in Table 1). The riverine sediments consisted of slow-settling

346 single fine grains (Class 4) and high-settling flocs (Class 5), which were delivered  
 347 into the model domain during both the 15-month spin-up period and the subsequent  
 348 12-month formal model experiments. The riverine flocs correspond to the flocculated  
 349 fractions of clay and silt, whereas the single fine grains represent the non-flocculated  
 350 components within the Pearl River-derived sediments, following the setting of [Bever](#)  
 351 [and MacWilliams \(2013\)](#). To clarify, at the start of the 12-month formal model  
 352 experiments, the retained Pearl River-derived sediments (Classes 4-5 in Table 1) that  
 353 entered the model during the 15-month spin-up period were added as Class 1 and  
 354 Class 2, respectively, to avoid contaminating the data analysis of the formal  
 355 experiments. This approach allows for a better distinction between Pearl River  
 356 sediment and seabed sediment, enabling separate analysis of the suspension, transport,  
 357 and deposition of Pearl River-derived sediment ([Harris et al., 2008](#); [Zhang et al.,](#)  
 358 [2019](#)). Specifically, the fractions of the two types of Pearl River-derived sediments  
 359 were set at 40% and 60%, respectively, following [Zhang et al. \(2019\)](#) and [Zhang et al.](#)  
 360 [\(2021\)](#). The parameters for all five sediment classes are summarized in Table 1.  
 361 Sediment density, porosity, and erosion rate for all sediment classes were set to 2650  
 362  $\text{kg m}^{-3}$ , 0.672 ([Zhang et al., 2019](#); [Zhang et al., 2021](#)), and  $1 \times 10^{-4} \text{ kg m}^{-2} \text{ s}^{-1}$  ([Ralston](#)  
 363 [et al., 2012](#)), respectively. The settling velocity ( $w_s$ ), critical shear stresses for erosion  
 364 ( $\tau_{ce}$ ), and other parameters were set following previous studies or were based on  
 365 model calibration ([Ralston et al., 2012](#); [Warner et al., 2017](#); [Zhang et al., 2019](#); [Dong](#)  
 366 [et al., 2020](#); [Zhang et al., 2021](#); [Cao et al., 2025](#)).



Our model configuration incorporates seasonal variations in  $\tau_{ce}$ , supported by multiple lines of evidence from field observations, laboratory experiments, and numerical analyses ([Dong et al., 2020](#); [Cao et al., 2025](#)). Previous studies have established a distinct seasonal pattern in the PRE, with winter  $\tau_{ce}$  values significantly exceeding those in summer. [Dong et al. \(2020\)](#)'s laboratory experiments using the UMCES-Gust Erosion Microcosm System (U-GEMS) on 2017-winter sediment samples yielded a  $\tau_{ce}$  of 0.26 Pa, which effectively reproduced observed suspended sediment concentration (SSC) in winter simulations. However, this value proved excessive for summer conditions, when a  $\tau_{ce}$  of 0.15 Pa provided better agreement with field observations in summer simulations, indicating a winter-to-summer  $\tau_{ce}$  ratio of 1.73. Recent 2020-summer in situ measurements by [Cao et al. \(2025\)](#) using a benthic quadrapod-mounted 3D Profiling Sonar revealed a two-layer erosion threshold system: a surface "fluffy layer" with  $\tau_{ce} = 0.06$  Pa overlying a consolidated seabed with  $\tau_{ce} = 0.13$  Pa. The latter value aligns with [Dong et al. \(2020\)](#)'s summer calibration, suggesting that [Dong et al. \(2020\)](#)'s laboratory measurements, potentially affected by sediment consolidation during sample transport, might have missed the lower  $\tau_{ce}$  of the surface fluffy layer. Based on these consistent findings, we implemented a seasonal  $\tau_{ce}$  adjustment factor of 1.73 (winter/summer) in our model configuration (Table 1).

**Table 1.** CSTM model Sediment Properties

Source	Seabed			Pearl River	
Class	1	2	3	4	5
Sediment Type	Clay	Silt	Sand	Single grains	Flocs
$w_s$ (mm s <sup>-1</sup> )	0.02 <sup>c</sup>	1.2	57 <sup>d</sup>	0.005 <sup>c</sup>	0.6
Summer $\tau_{ce}$ (Pa)	0.14 <sup>e</sup>	0.03	0.27 <sup>d</sup>	0.15 <sup>abef</sup>	0.05 <sup>abe</sup>
Winter $\tau_{ce}$ (Pa)	0.24 <sup>f</sup>	0.05 <sup>f</sup>	0.47 <sup>df</sup>	0.26 <sup>abf</sup>	0.09 <sup>abf</sup>
Fraction	Spatially variable, see Figure 2g-i			40% <sup>ab</sup>	60% <sup>ab</sup>

<sup>a</sup>Zhang et al. (2019), <sup>b</sup>Zhang et al. (2021), <sup>c</sup>Calibrated, <sup>d</sup>Warner et al. (2017), <sup>e</sup>Cao et al. (2025), and <sup>f</sup>(Dong et al., 2020).

## 2.5 Wet and dry season regimes

The study area exhibits pronounced seasonal variability, which can be distinctly categorized into two primary seasons (Dong et al., 2004; Su, 2004; Liu et al., 2014; Zhang et al., 2021). This seasonal classification is supported by multiple environmental parameters, including river freshwater discharge, riverine sediment load (Figure 3a), wind patterns (Figure 3b), air temperature (Figure 3c), and modeled wave conditions (Figure 3d-f) at a representative site (21.5°N, 114°E; corresponding to station W1 in Figure S1a, located immediately south of the PRE). The meteorological data for wind and air temperature were obtained from the NCEP reanalysis dataset, while wave parameters were derived from numerical model simulations. These comprehensive indicators collectively characterize the distinct seasonal patterns observed in the study area (Figure 3). The entire year (from April 1,

2017, to March 31, 2018) is typically divided into two main seasons: wet summer (from April 1, 2017, to September 30, 2017) and dry winter (from October 1, 2017, to March 31, 2018).

During the wet summer season, freshwater discharge tends to be notably high, often exceeding  $10,000 \text{ m}^3 \text{ s}^{-1}$  and reaching a maximum of  $53,000 \text{ m}^3 \text{ s}^{-1}$ , with an average value of  $15,266 \text{ m}^3 \text{ s}^{-1}$ . This discharge constitutes a significant portion of the entire year, accounting for 72.06% of the annual total. During this period, the river carries a substantial sediment load of 32.85 megatons, constituting 95.17% of the total annual sediment transport. Prevailing winds predominantly blow from the south. For example, Figure 3b depicts the average monthly wind vector direction during the summer months as northward, with weak southeasterly winds in April, May, and September, and moderate southeasterly winds in July. June and August experience moderate southwesterly winds. The 2 m height air temperatures typically range between  $20^\circ\text{C}$  and  $30^\circ\text{C}$ . The daily average  $H_{\text{sig}}$  remains relatively low, with the monthly average  $H_{\text{sig}}$  less than 1 m. The wave propagation direction is generally consistent with the wind direction, being easterly in April and May, and southerly from June to September.

In stark contrast, the dry winter season demonstrates markedly lower runoff, typically falling below  $10,000 \text{ m}^3 \text{ s}^{-1}$ , with an average value of  $5,953 \text{ m}^3 \text{ s}^{-1}$ . The sediment load during this period is significantly reduced to merely 1.67 megatons, marking a substantial decrease compared to the wet summer season. Prevailing winds during the dry winter are predominantly northeasterly, with relatively high wind

speeds. Except for moderate wind intensity in March, the monthly average wind speed in other months exceeds  $5 \text{ m s}^{-1}$ . The 2 m height air temperatures typically range between  $10^{\circ}\text{C}$  and  $25^{\circ}\text{C}$  during this season. The wave propagation direction aligns with the prevailing northeasterly winds of the season, predominantly northeasterly.

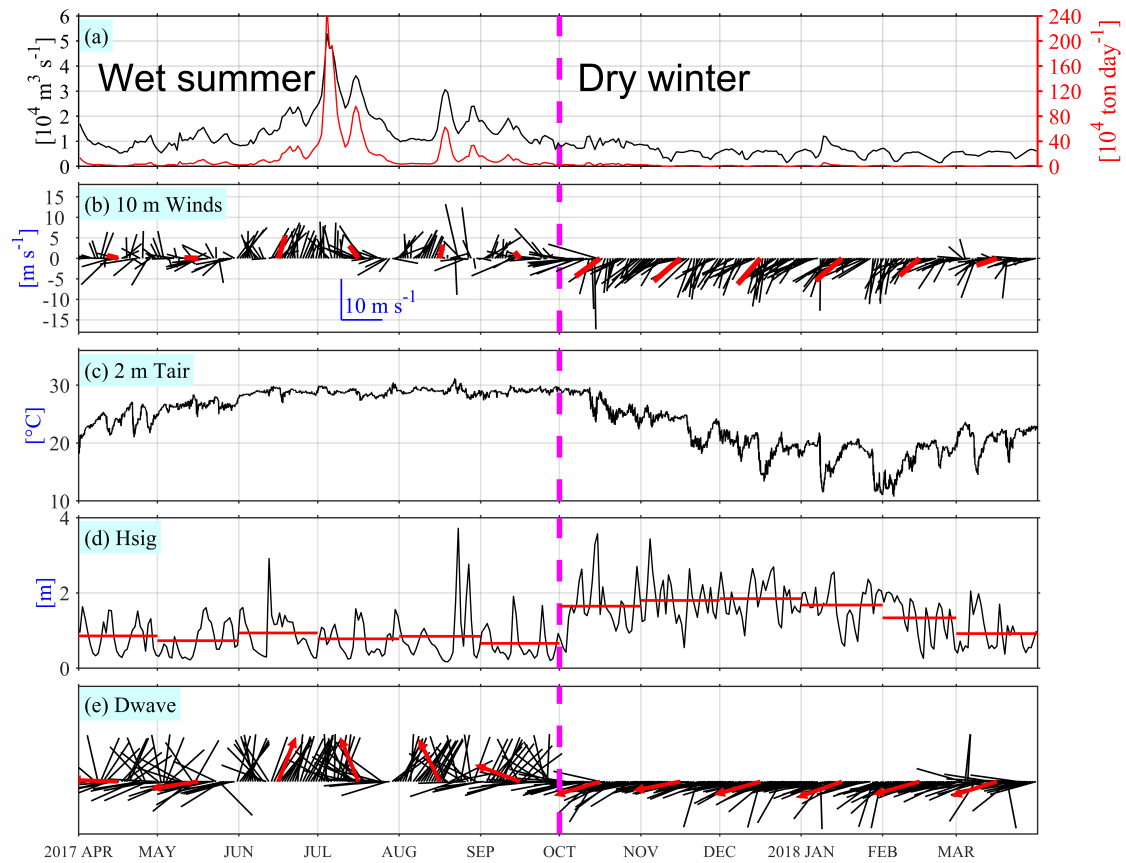


**Figure 3.** Time series of (a) the daily Pearl River freshwater discharge and sediment load, (b) daily (black vectors) and monthly (red vectors) averaged 10-meter height winds, (c) hourly 2-meter height air temperature, daily (black) and monthly (red) averaged (d) significant wave height ( $H_{sig}$ , lines) and (f) wave propagation direction (vectors) weighted by  $H_{sig}^2$ . Two distinct seasons are delineated by the dashed magenta line.

437

## 438 **2.6 Model experiments**

439 To assess the relative importance of tides, waves, ambient shelf currents and  
440 residual water levels, seasonal variation in critical shear stress for erosion, the settling  
441 velocity, and the spin-up duration of Pearl River-derived sediment (Classes 4-5 in  
442 Table 1) in the transport and dispersal of Pearl River-derived sediments, we conducted  
443 seven simulation experiments (Table 2). In all experiments, we implemented the  
444 Charnock approach within COAWST's bulk air-sea flux parameterization scheme to  
445 calculate surface wind stress using the NCEP 10-m wind product ([Charnock, 1955](#);  
446 [Fairall et al., 1996](#)), ensuring consistency in wind stress forcing across all simulations.

447 Exp 1 (the **Control** run) incorporated all the aforementioned forcing agents  
448 (including winds) and accounted for the seasonal variation in critical shear stress for  
449 erosion, with the winter critical shear stress for erosion set to be 1.73 times of that in  
450 summer. Exp 2 (**NTS** hereafter) was identical to Exp 1 but excluded tides, while Exp  
451 3 (**NWS** hereafter) excluded waves. In Exp 4 (**NAS** hereafter), waves, tides, and the  
452 seasonal variation in critical shear stress for erosion were included, but the shelf  
453 current and residual water levels were omitted (i.e., no subtidal circulation forcing at  
454 open boundaries) to examine the influence of the South China Sea circulation. Exp 5  
455 (**NVS** hereafter) replicated the setup of Experiment 1, but with one modification: it  
456 used a constant critical shear stress for erosion ( $\tau_{ce}$ ) across both seasons, specifically  
457 adopting the summer  $\tau_{ce}$  value from Table 1 throughout the simulation (i.e., no  
458 seasonal adjustment between winter and summer). Exp 6 (**DSV** hereafter) was

identical to Exp 1, except that it set a double sediment settling velocity of the Exp 1. Finally, to assess the model's sensitivity to the spin-up duration of Pearl River-derived sediment, particularly regarding the retention of riverine sediments in both the water column and the seabed, we adopted the sediment distributions (Classes 1 to 5) from the Control run on March 31, 2018, as the alternative initial conditions for the Cycle experiment (designated as Exp 7, **Cycle** hereafter). This setup carries over the full year's evolution of riverine sediment transport and deposition from the Control run (Exp 1), including changes in all sediment classes, into the start of Exp 7. As a result, Exp 7 mainly evaluates how the presence of previously deposited riverine sediments influences subsequent sediment transport estimates.

**Table 2.** Experiment Settings

Experiments	Tides	Waves	Ambients	$\tau_{ce}$	$w_s$	Re-run
Exp 1 (Control)	✓	✓	✓	Variable	Original	✗
Exp 2 (NTS)	✗	✓	✓	Variable	Original	✗
Exp 3 (NWS)	✓	✗	✓	Variable	Original	✗
Exp 4 (NAS)	✓	✓	✗	Variable	Original	✗
Exp 5 (NVS)	✓	✓	✓	Constant	Original	✗
Exp 6 (DSV)	✓	✓	✓	Variable	Double	✗
Exp 7 (Cycle)	✓	✓	✓	Variable	Original	✓

The term 'Ambients' denotes ambient shelf currents and residual water levels. Variable indicates simulations employing seasonally varying  $\tau_{ce}$  values (from Table 1), while

'Constant' refers to runs using exclusively the summer  $\tau_{ce}$  value throughout the entire experiment. 'Original' designates cases utilizing the settling velocities specified in Table 1, whereas 'Double' indicates simulations with these values doubled."

## **3 Results**

### **3.1 Seasonal hydrodynamics and transport patterns of the Pearl**

#### **River-derived sediment**

We quantified the spatial distributions of seasonal mean wind stress,  $H_{sig}$ , wave bottom orbital velocity (WBOV), and bottom shear stress for both the wet summer and dry winter periods (as defined in Section 2.5). These distributions serve as representative hydrodynamic conditions for typical summer and winter scenarios, respectively (Figure 4).

During summer, the prevailing winds predominantly originate from the south, with the average wind stress generally below 0.03 Pa, except in the eastern coastal waters of Hainan Island, where localized values reach up to 0.05 Pa (Figure 4a). In contrast, during the dry winter season, the prevailing winds shift to a northeasterly direction, resulting in generally higher average wind stress compared to summer (Figure 4b), with values typically exceeding 0.1 Pa in areas deeper than 40 m and surpassing 0.2 Pa in the offshore eastern Guangdong Coast near the Taiwan Bank (see Figure 1).

Corresponding to the seasonal wind stress (Figures 4a-b), the seasonally averaged

wave characteristics in the PRE and the adjacent northern continental shelf of the South China Sea exhibit significant seasonal variations (Figures 4c-d).

During the wet summer season, the Hsig in the studied area is relatively low, with waves predominantly coming from the southeast (Figure 4c). The seasonal average Hsig across the entire shelf remains below 1 m, with areas deeper than 60 m showing Hsig values above 0.8 m, while in shallower nearshore regions (water depth < 20 m), Hsig is less than 0.6 m (Figure 4c). Corresponding to the lower Hsig in the wet summer, the seasonally-averaged WBOV is also relatively small, generally less than 1 cm s<sup>-1</sup> in areas deeper than 40 m, except in some nearshore shallow water regions where it reaches up to 10 cm s<sup>-1</sup> (Figure 4e). The seasonally-averaged bottom shear stress during the wet summer is relatively high in the PRE, nearshore regions, and the Taiwan Bank, where tidal dissipation is strong (Figure 4g).

In the dry winter season, the Hsig increases significantly compared to the wet summer, with waves primarily coming from the northeast, although refraction occurs in some nearshore regions, changing the wave direction to southeasterly (Figure 4d). The area with water depths exceeding 60 m has a Hsig greater than 1.5 m, while in the 20-meter depth region, the Hsig reaches approximately 1 m (Figure 4d). Compared to the wet summer, the WBOV increases significantly in the PRE mouth and many nearshore regions, reaching up to 10-20 cm s<sup>-1</sup> (Figure 4d). The average bottom shear stress on the continental shelf outside the estuary also increases significantly during the dry winter compared to the wet summer (Figure 4f).



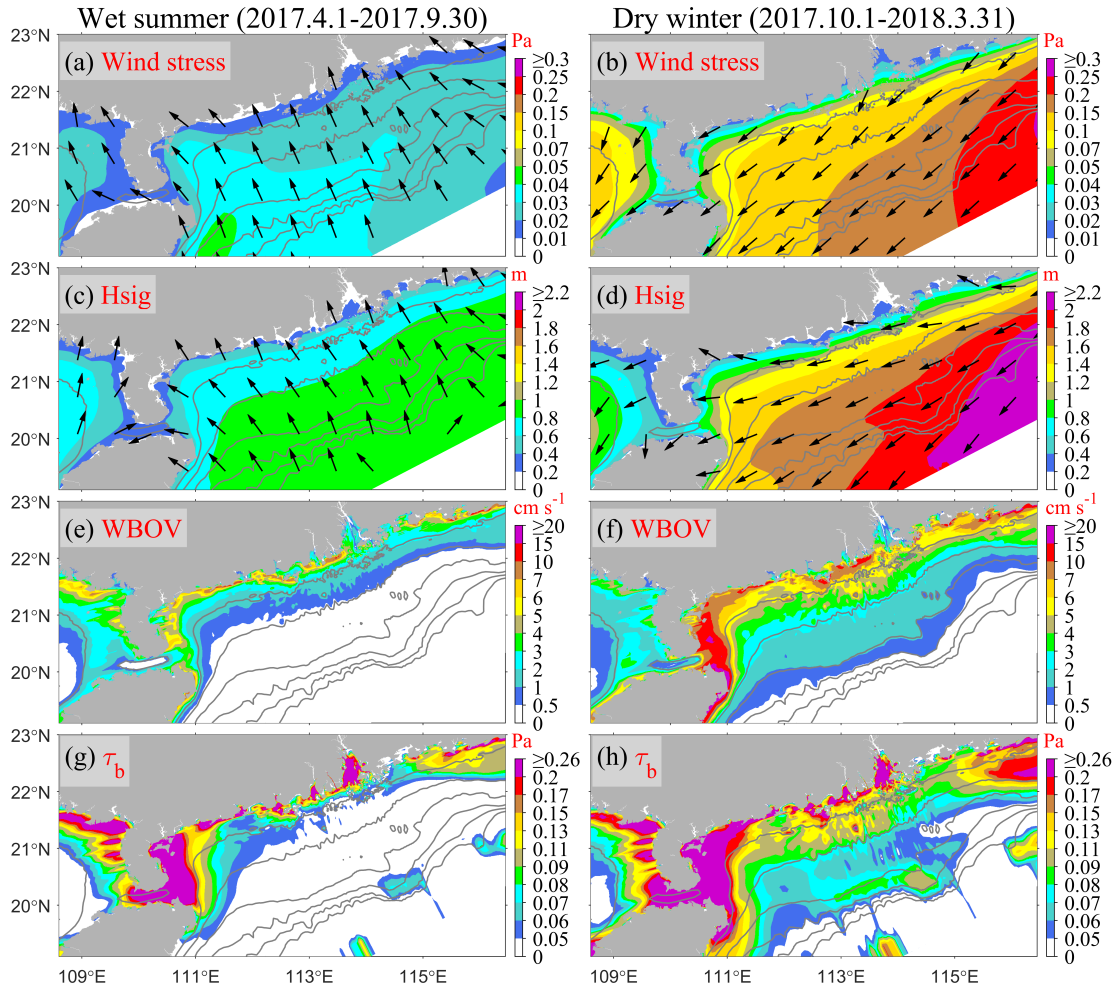


**Figure 4.** The patterns of variables averaged for the wet summer season (April 1st to September 30th, 2017; Column 1) and the dry winter season (October 1st to March 31st, 2018; Column 2) in the Control case. Row 1 (a-b) depicts wind stress (color) and direction (vectors), Row 2 (c-d) shows Hsig (color) and propagation direction (vectors) weighted by Hsig<sup>2</sup>, Row 3 (e-f) presents wave bottom orbital velocity (WBOV), and Row 4 (g-h) displays bottom shear stress magnitude.

The patterns of residual sediment dispersal, flux, and deposition over the simulation period provide clear information on the mechanisms for sediment redistribution on both annual and seasonal timescales. The following section presents

a detailed analysis of the seasonally averaged fields of salinity, flow, riverine SSC, depth-integrated riverine sediment flux, and riverine sediment deposition patterns during the wet summer season (Figure 5) and dry winter season (Figure 6) on the continental shelf.

During the wet summer season, when freshwater discharge is high and water column stratification is strong, riverine SSC (“riverine” means only Pearl River-derived sediment, classes 4-5 in Table 1, as follows) is primarily influenced by advection from the buoyant river plume (salinity less than 33.5 in Figure 3a, as follows) into the shelf sea, primarily in the surface layer (Figures 5a-b), high SSC regions closely align with the buoyant plume, as sediment is efficiently transported by the low-salinity, high-momentum freshwater outflow (Figures 5a-d). The buoyant plume extends both northeastward and southwestward along the coastline (Figure 5a). Due to the influence of southerly winds (Figure 4a) and ambient shelf currents, the extent of the buoyant plume extending northeastward is significantly higher than that extending southwestward. In terms of riverine sediment suspension, its estuarine turbidity maxima (ETM) zone ( $\sim 100 \text{ mg L}^{-1}$ ) is situated in the shallow water area within the estuary (water depth  $< 10 \text{ m}$ ) (Figure 5c-d). Beyond the estuary, suspended riverine sediment disperses across the shelf through the buoyant plume. Further away from the estuary, its distribution aligns with that of the buoyant plume, with concentrations diminishing as dispersal distance increases. The depth-integrated advective horizontal flux (without including vertical processes such as settling, resuspension, or diffusion, which are handled separately within the model) of riverine

550 sediment offers a clear indication of the primary net transport pathway of the riverine  
551 sediment (Figure 5e). The riverine sediment exhibits both southwestward and  
552 northeastward fluxes (Figure 5e). Southwestward coastal transport can extend as far  
553 as the Leizhou Peninsula and Hainan Island. On the eastern side, the northeastward  
554 transport extends toward the Taiwan Bank. However, the primary transport pathway  
555 there is diverted southward (Figure 5e) due to the obstruction caused by summer  
556 upwelling near the Guangdong east coast ([Chen et al., 2017a](#); [Chen et al., 2017b](#)), as  
557 evidenced by the cross-shore current in the bottom layer (Figure 5b). The  
558 southwestward transport pathway follows the region where the water depth is  
559 shallower than 30 m, with a riverine sediment flux of  $10\text{--}20\text{ g m}^{-1}\text{ s}^{-1}$ . In contrast, the  
560 northeastward transport pathway occurs in the 30–60 m depth range, but the riverine  
561 sediment flux is below  $10\text{ g m}^{-1}\text{ s}^{-1}$ . Throughout the wet summer season, substantial  
562 amounts of riverine sediment are deposited near the estuary (Figure 5d), particularly  
563 leading to notably high deposition of riverine sediment near the river mouth ( $> 100$   
564 mm). Outside the estuary, the thickness of riverine sediment is comparatively lower,  
565 but it can reach approximately  $\sim 0.5$  mm during the wet summer season in certain  
566 areas off the western Guangdong coast.

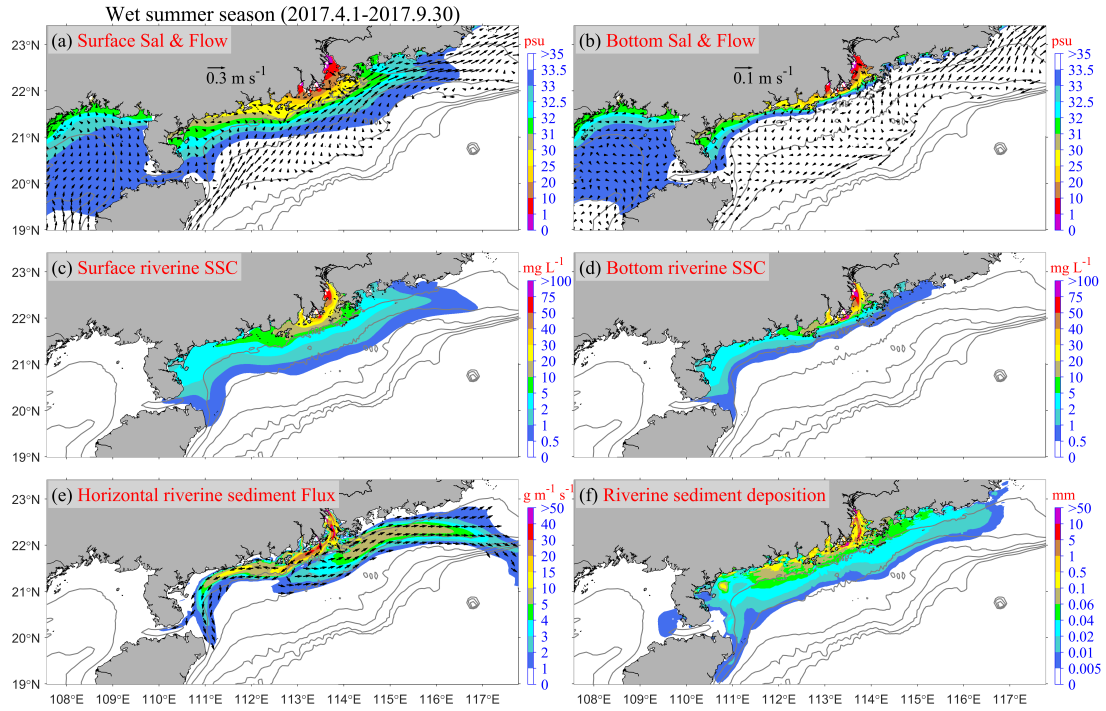


**Figure 5.** Patterns averaged over the entire wet summer season in the Control case: (a) surface and (b) bottom salinity (color, psu) and flow (arrows,  $\text{m s}^{-1}$ ); (c) surface and (d) bottom riverine (classes 4 and 5 in Table 1, as follows) SSC ( $\text{mg L}^{-1}$ ); (e) depth-integrated horizontal riverine sediment transport rate (color,  $\text{g m}^{-1} \text{s}^{-1}$ ) and direction (arrows); and (f) riverine sediment deposition thickness (mm) on the seabed during the wet summer season. Flow vectors in regions with water depths exceeding 100 m are masked for clarity.

In contrast, during winter, when river discharge is low and vertical mixing is more intense, the correlation between the buoyant plume and riverine SSC is much weaker, and the riverine SSC is largely governed by resuspension processes driven by strong northeasterly winds and waves, rather than by freshwater transport. The

expansion of the Pearl River buoyant plume is constrained to the southwestward direction by strong northeasterly winds (Figure 6a), resulting in a narrow cross-shore width of the buoyant plume and the formation of a strong horizontal salinity gradient (i.e., a salinity front, particularly within the 30–33.5 psu range shown in Figure 6a) outside the estuary (Figure 6a). Flow velocity increases near this salinity front, facilitating the westward extension of the buoyant plume through the Qiongzhou Strait into the "Gulf" region. The riverine SSC is significantly lower than in the wet summer: in the ETM zone inside the PRE, riverine SSC falls from roughly 100 mg L<sup>-1</sup> in summer to about 10 mg L<sup>-1</sup>, while on the offshore shelf, it decreases from approximately 5 mg L<sup>-1</sup> to around 2 mg L<sup>-1</sup> (Figures 6c-d vs. 5c-d). During the dry winter, following the coastal current, the riverine suspended sediment primarily moves southwestward along the coast, deflecting southward along the topography near the Leizhou Peninsula (Figure 6c). It then bifurcates near the east entrance of the Qiongzhou Strait, with one branch continuing into the "Gulf" region, and the other one proceeding southward along the east coast of Hainan Island. Stronger winds and waves in the dry winter lead to the resuspension of a considerable amount of riverine sediments, originally deposited in "Proximal", "Western", and "Eastern" regions during summer. The resuspended sediments are then transported to coastal bays as well as to the sides and rears of the islands (Figure 6d). Additionally, a portion of the riverine sediment transported to the "Gulf" region gets deposited on the seabed during the dry winter season.

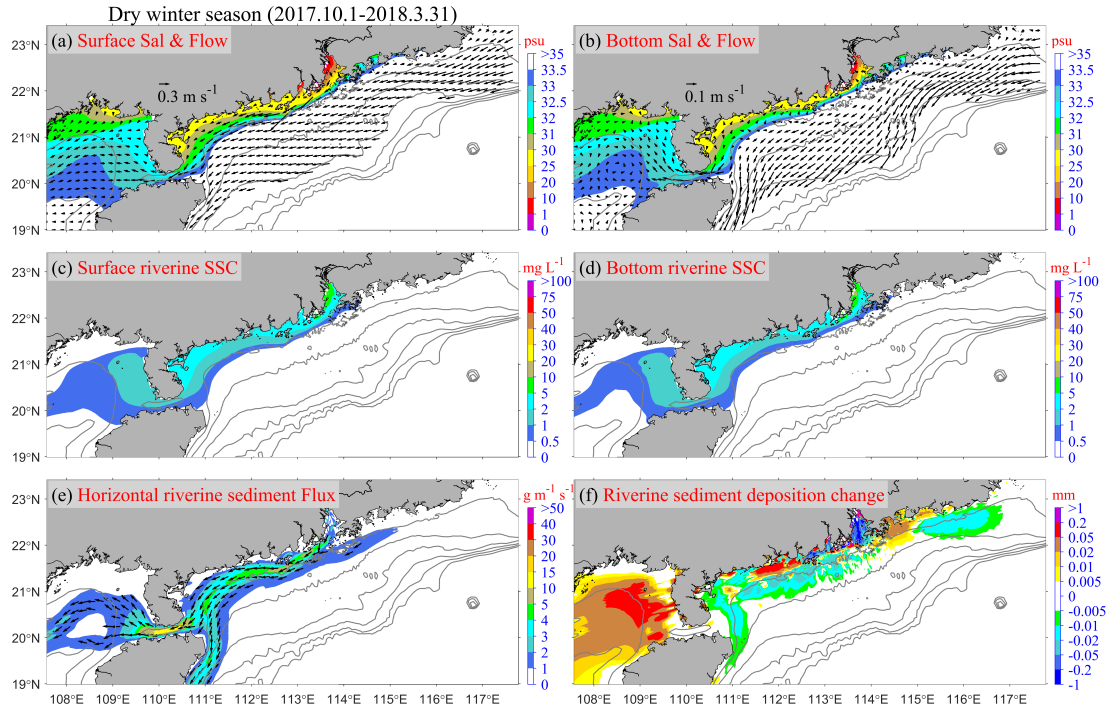


**Figure 6.** Same as Figure 5, but for the dry winter season in the Control case. Notably, (f) illustrates the changes in riverine sediment (classes 4 and 5 in Table 1) deposition on the seabed at the end of the dry winter season compared to the end of the wet summer season.

### 3.2 Riverine sediment budgets and annual deposition over the shelf

We present the sediment fluxes and retention amounts in different regions. Figure 7a-c illustrates the proportion of riverine sediment retention budget within each region, expressed as a percentage of the total annual river sediment input, for the wet summer season, the dry winter season, and the entire year under the Control run case, respectively. Meanwhile, Figure 7d illustrates the annual deposition over the shelf.

The retention of Pearl River sediment on the continental shelf exhibits significant

617 seasonal variations (Figures 7a-c). During summer (characterized by high discharge  
618 and low wind/waves), the PRE and continental shelf receive 95.17% of the annual  
619 sediment load from the Pearl River (Figures 3a and 7a). Approximately two-thirds of  
620 this sediment is retained in the "Proximal" region (Figure 7a). Additionally, influenced  
621 by the prevailing southerly winds and northeastward shelf circulation, 13.01% of the  
622 annual sediment load is retained in the "Eastern" and "Southeastern" regions (Figure  
623 7a). Meanwhile, the shelf west of the PRE (⑤–⑧ regions) retains 15.87% of the  
624 annual load, with the "Western" region being the primary receiver, accounting for 8.48%  
625 (Figure 7a). Only 0.92% and 2.3% of the annual load enter the "Gulf" and "Distal"  
626 regions, respectively, during summer (Figure 7a). The "Southern" region retains a  
627 mere 1.22% of the sediment (Figure 7a). In winter (characterized by low discharge  
628 and energetic winds/waves), the PRE and the continental shelf receive only 4.83% of  
629 the annual sediment load (Figures 3a and 7b). The sediment distribution during this  
630 season is primarily a result of the dynamic reworking of the sediments of summer  
631 deposition (Figure 7b). While the "Proximal" region continues to receive sediment,  
632 with a 1.38% increase in retention, the ②–⑥ regions experience a decrease in  
633 sediment retention. This sediment is predominantly transported and retained in the  
634 more distant "Gulf" and "Distal" regions (Figure 7b). The annual sediment budget  
635 reveals that 66.45% of the Pearl River sediment is retained in the "Proximal" region  
636 (Figure 7c). Additionally, 9.2% is retained in the "Eastern" and "Southeastern" regions  
637 (Figure 7c), primarily during summer (Figures 7a vs. 7c), while 24.12% is retained on  
638 the shelf west of the PRE (⑤–⑧ regions), with the majority in the "Gulf" and





**Figure 7.** Riverine sediment (classes 4 and 5 in Table 1) retention budget percentages at eight regions (see Figure 1) during (a) the wet summer season, (b) the dry winter season, and (c) the entire year in the Control run case. (d) the annual deposition patterns spanning from April 1st, 2017, to March 31st, 2018 in the Control Run. All percentages displayed in the figure are relative to the annual riverine sediment load (see Figure 3a). The black percentage values represent the combined total of riverine sediment Class 4 and Class 5, while the red and blue values denote sediment Class 4 and Class 5, respectively. Arrows indicate the direction of net riverine sediment flux at each transect during the specified period.

### **3.3 Model sensitivity experiments: relative roles of physical processes, sediment properties, and spin-up durations**

Six sensitivity simulations, namely Exp 2-7 (NTS, NWS, NAS, NVS, DSV, and Cycle), were conducted (Table 2). As the latter three experiments do not impact hydrodynamics, we focus on presenting the seasonal mean differences in bottom shear stress between the Control run and the first three cases (NTS-Control, NWS-Control, NAS-Control) for both summer and winter (Figure 8).

In the NTS case, bottom shear stress is reduced relative to the Control run by a similar amount in both summer and winter due to the minimal seasonal variation in tidal intensity. This reduction primarily occurs in the PRE, around the Taiwan Bank, and near the Leizhou Peninsula (Figures 8a-b). In contrast, in the NWS case, the reduction in bottom shear stress is greater in winter than in summer, reflecting the

675 intense seasonal variability of wind and wave activities (Figures 3b, 3d-e, and 4a-f).  
676 Unlike the NTS case, the NWS-induced decrease occurs mainly in the nearshore areas  
677 outside the PRE, although similar declines are also found around the Taiwan Bank and  
678 along the eastern side of the Leizhou Peninsula (Figures 8c-d). For the NAS case, the  
679 impact on bottom stress is minimal compared to the NTS and NWS cases. The effect  
680 is almost negligible on the inner shelf at depths less than 100 m, with widespread  
681 impacts generally below 0.02 Pa. Some pronounced deviations are noted in localized  
682 deeper areas near the southern boundary of the domain (Figures 8e-f). These  
683 deviations, likely arising from boundary condition effects, are situated far from the  
684 Pearl River-derived sediment distribution areas (Figures 5-6). Consequently, they do  
685 not influence the dynamics of the Pearl River-derived sediment transport over the  
686 continental shelf (Figures 8e-f).  
687

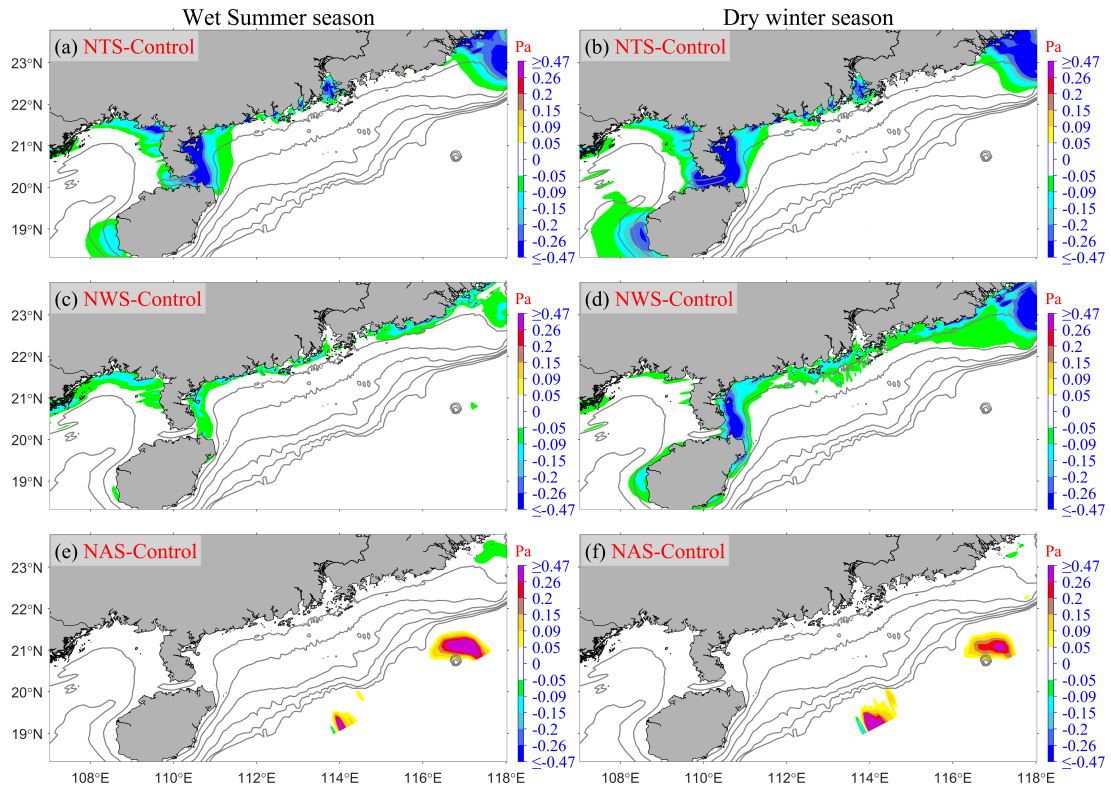


**Figure 8.** The seasonal mean differences in bottom shear stress between the Control run and the following cases: (a-b) NTS (NTS minus Control), (c-d) NWS (NWS minus Control), and (e-f) NAS (NAS minus Control). The first column represents the wet summer season, while the second column corresponds to the dry winter season.

Then, we analyzed seasonal riverine sediment transport and deposition patterns (“riverine” means only the Pearl River-derived sediment, classes 4-5 in Table 1, as follows) by comparing the control run with six sensitivity experiments (NTS-Control, NWS-Control, NAS-Control, NVS-Control, DSV-Control, and Cycle-Control) (Figures 9-11). The study focuses on the Pearl River-derived sediment dynamics, indicated by surface circulation and riverine SSC distribution patterns (Figures 5 and 6). Specifically, Figures 9 and 10 present seasonal surface currents and SSC

differences between control and sensitivity runs, complemented by deposition pattern differences in Figure 11.

Compared to the Control case, the NTS case demonstrates that while tides significantly enhance bottom stress (Figures 8a-b) but have minimal impact on the mean circulation (Figures 5a, 6a, and 9a-b), and their exclusion reduces bottom shear stress by over 0.2 Pa in the PRE and near the Leizhou Peninsula. Consequently, increased deposition of the Pearl River-derived sediments occurs inside the PRE, its adjacent areas, and on both sides of the Leizhou Peninsula (Figure 11a). During summer, riverine SSC notably decreases in the ①–⑥ regions (Figure 9a). This reduction pattern persists in winter, particularly in the PRE and on both sides of the Leizhou Peninsula (Figure 9b).

Like the NTS, NWS has a relatively minor impact on circulation (Figures 5a, 6a, and 9c-d). However, NWS leads to more Pearl River-derived sediment being deposited in the nearshores of “Western” and “Eastern” regions (Figure 11b). Consequently, the riverine SSC in summer is much lower in the downstream of the PRE and in ②–⑥ regions (Figure 9c). This similar reduction pattern persists in the winter, but is slightly in more western regions (Figure 9d).

For the NAS case, the impact on bottom stress is minimal compared to the NTS and NWS cases. However, NAS has a relatively large impact on the mean circulation (Figures 5a, 6a, and 9e-f). It mainly influences the summer circulation. Specifically, ignoring these factors would cause the relatively strong northeastward flow along the Guangdong coast to become very weak (Figure 9e). When it comes to winter, the

influence of NAS on circulation is relatively small. That is, in the absence of the background residual water level and residual circulation, due to the strong northeasterly winds in winter, the overall circulation is still southwestward (Figure 9f). The decreased northeastward flow in summer leads to the Riverine SSC being scarcely transported to the vicinity of the “Eastern” and “Southeastern” regions. Consequently, the Riverine SSC there is decreased (Figure 9e) and sediment deposition is significantly reduced (Figure 11c). Most of the suspended Riverine sediment is transported southwestward, resulting in an increase in the Riverine SSC along the “Western” region. In winter, since most of the suspended Riverine sediment has been transported southwestward in summer, the Riverine SSC decreases compared to the Control run (Figure 9f). Ultimately, NAS mainly causes a significant reduction in sediment deposition in the “Eastern” region, while sediment deposition increases in the "Gulf" and the "Distal" regions (Figure 11c).

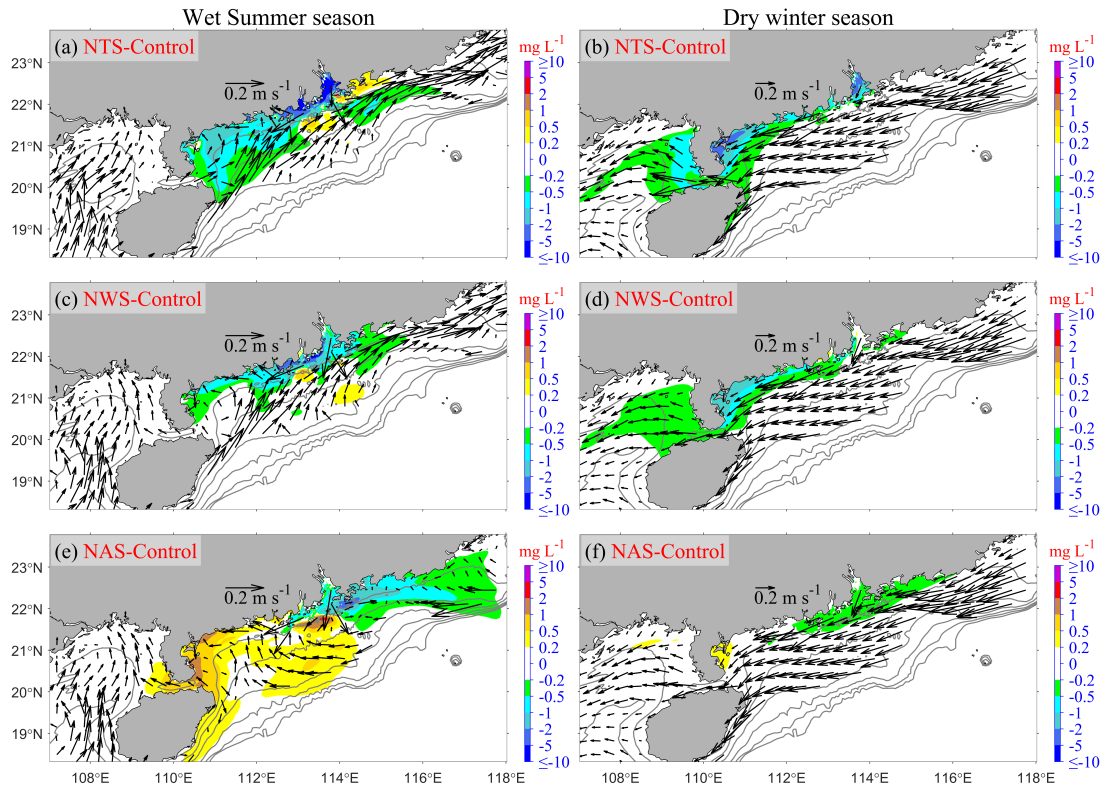


**Figure 9.** Same as Figure 8, but for seasonal mean differences in surface riverine SSC between the Control run and the following cases: (a-b) NTS-Control, (c-d) NWS-Control, and (e-f) NAS-Control. The first column represents the wet summer season, while the second column corresponds to the dry winter season. Vectors show the seasonal mean surface current fields in each experiment. Note that the riverine SSC values shown in the figure correspond to classes 4 and 5 as defined in Table 1.

For the NVS case, the summer conditions of NVS are precisely the same as those of the Control run (Figure 10a). Since the critical shear stress for erosion in winter is lower than that in the Control run, this leads to an increase in re-suspension in the “Proximal”, “Western” and the “Gulf” regions, increasing Riverine SSC (Figure 10b).

Eventually, this causes a reduction in the deposition thickness of the Pearl River-derived sediments in these regions(Figure 11d).

In the DSV case, significant reductions occur in the primarily high SSC areas in the Control run in both summer and winter (Figures 5c, 6c, 10c-d). The enhanced settling velocity results in an increased deposition of Pearl River-derived sediments along the Guangdong coastline ("Western" and "Eastern" regions) and the eastern "Gulf" region, accompanied by a reduced deposition thickness in the western "Gulf" region (Figure 11e).

In the Cycle case, the new riverine sediment input and its transport processes during the Cycle experiment are nearly identical to those in the Control run. Therefore, compared to the Control run, the Cycle experiment specifically focuses on examining the impact of the presence of pre-existing Pearl River-derived sediments on estimating the riverine SSC and the annual seabed riverine sediment budget in the second year. Consequently, during the summer period, the Cycle case experiences elevated riverine SSC in the primary depocenters identified in the Control run (Figures 7d and 10e), while this effect is diminished by winter (Figure 10f). Figure 11f thus captures the transport trends of pre-existing riverine sediments in the second year, demonstrating that riverine sediments deposited during the first year can be resuspended and transported further southwestward during the second year. This migration is driven by the annually averaged net alongshore coastal current, which remains predominantly directed toward the southwest. The current becomes stronger during the winter monsoon under the influence of prevailing northeasterly winds, whereas the opposing

summer southerly winds are comparatively weaker, indicating a persistent southwestward sediment transport trend over multi-year timescales.

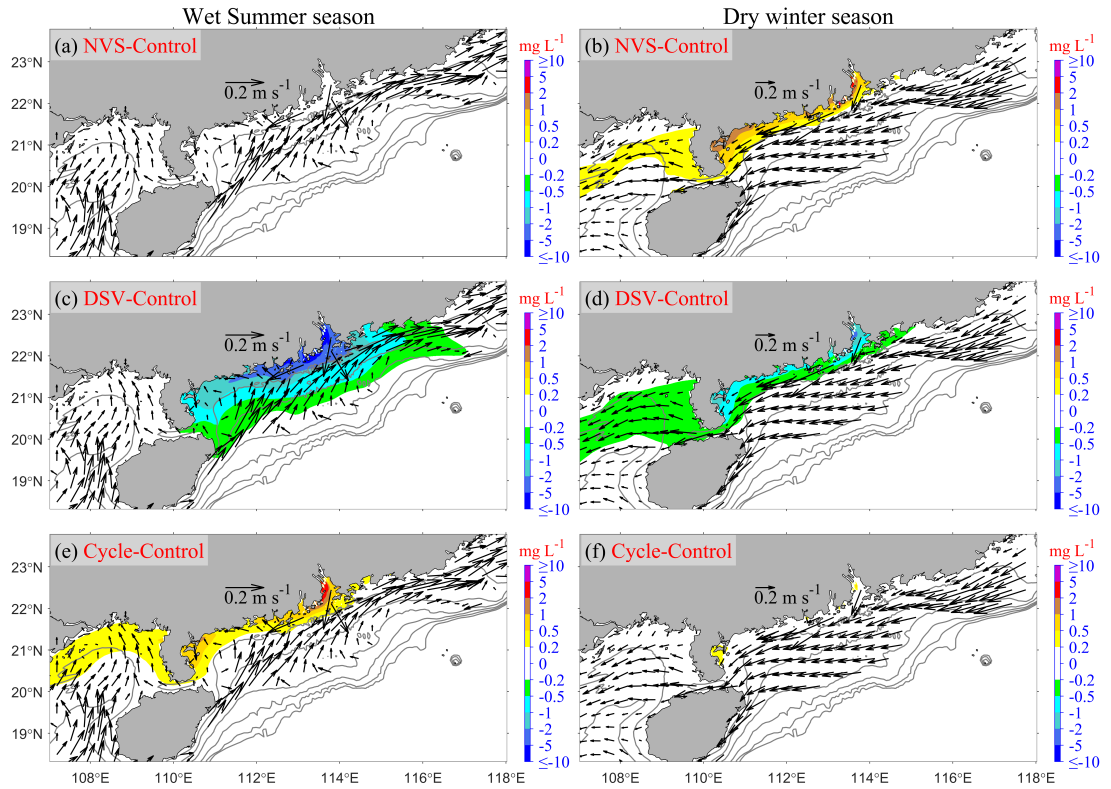


**Figure 10.** Same as Figure 9, but for the latter three experiments (NVS, DSV, Cycle). (a-b) NVS-Control, (c-d) DSV-Control, and (e-f) Cycle-Control.



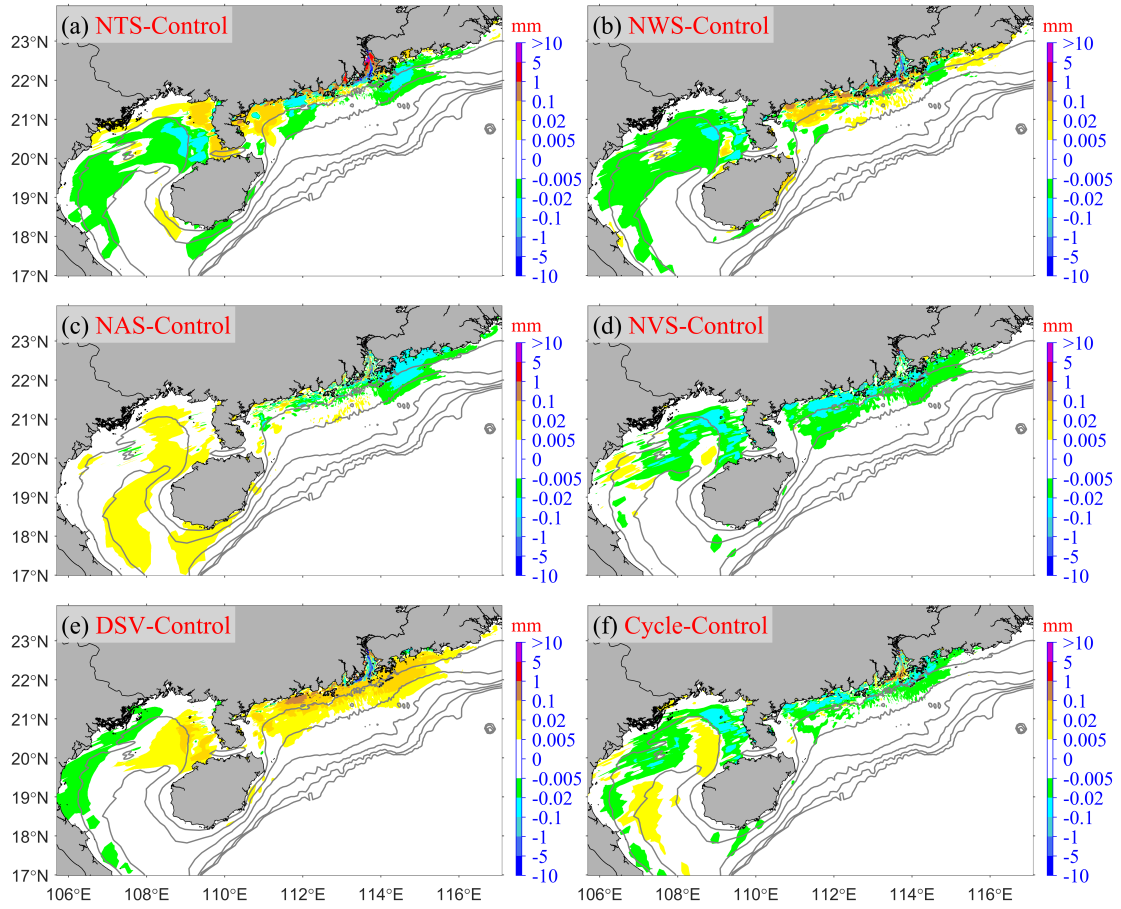


**Figure 11.** The differences in annual deposition patterns of Pearl River-derived sediment (classes 4-5, Table 1) on the seabed between the Control run and the following cases: (a) NTS-Control, (b) NWS-Control, (c) NAS-Control, (d) NVS-Control, (e) DSV-Control, and (f) Cycle-Control.

### 3.4 Modeled regional retention budgets in sensitivity experiments

Finally, we analyze the impact of various factors on the annual riverine sediment retention budget across different regions. Specifically, Figure 12 illustrates the annual riverine sediment retention budget in various regions under six sensitivity simulations, namely Exp 2-7 (including NTS, NWS, NAS, NVS, DSV, and Cycle). It should be

noted that the retention percentages budget and their variations discussed hereinafter are all relative to the annual riverine sediment load (Figure 3a).

As shown in Figure 12, tides and sediment settling velocity have the most significant impact on the retention in the "Proximal" region. In the NTS case and the DSV case, the retention in the "Proximal" region is 70.92% and 71.57%, respectively (Figures 12a and 12e), which is higher than 66.45% in the Control run (Figure 7c). This indicates that ignoring tides will cause the "Proximal" region to capture more riverine sediments, and a larger settling velocity will result in more riverine sediments being retained within the "Proximal" region. In these two cases, compared with the Control run, the retention in the "Gulf" and "Distal" regions decreases. Meanwhile, the DSV case causes the greatest increase in retention in the "Western" region, with an increase of +1.91%.

Furthermore, the NWS also leads to a 2.2% increase in retention in the "Proximal" region (Figure 12b), which is lower than that in the NTS case. This shows that tides dominate resuspension versus deposition in the "Proximal" region more than waves do. However, for the "Western" region, compared with the NTS case, the NWS causes a greater increase in retention, indicating that waves dominate the resuspension of Pearl River-derived sediments in these nearshore areas more than tides do.

For the "Eastern" and "Southeastern" regions, NAS brings about the most dramatic changes, the retention of Pearl River-derived sediments in these regions drops from 9.1% to 0.84% compared to the Control run (Figure 12c). Meanwhile, ignoring these background circulations results in a substantial increase in the retention

in the "Distal" region, with an increase of 6.49%.

The NVS case leads to a decrease in the retention of the Pearl River-derived sediments in ①–⑥ regions compared to the Control run. The reduction ranges from -0.05% to -0.85% (Figure 12d), which in turn causes the retention in the "Gulf" and "Distal" regions to increase by 0.7% and 1.47%, respectively. Overall, compared with scenarios that ignore physical processes and alter sediment settling velocity (NTS, NWS, NAS, and DSV), the NVS scenario has a relatively smaller impact on the retention of the Pearl River-derived sediments.

Finally, in the Cycle case, to isolate the pre-existing Pearl River-derived sediments, the initial retentions (the end conditions of the Control run on March 31, 2018) were subtracted before calculating the retention in the Cycle case (Figure 12f). The retention of Pearl River-derived sediments in ①–⑥ regions shows little variation, with values ranging from -0.98% to +0.24% compared to the Control run (Figure 12f). The most significant changes are the decreases and increases in retention in the "Gulf" and "Distal" regions, which are -2.17% and +3.54%, respectively. This demonstrates the long-term trend of southwestward transport of Pearl River-derived sediments on the shelf (relative to the Control run).

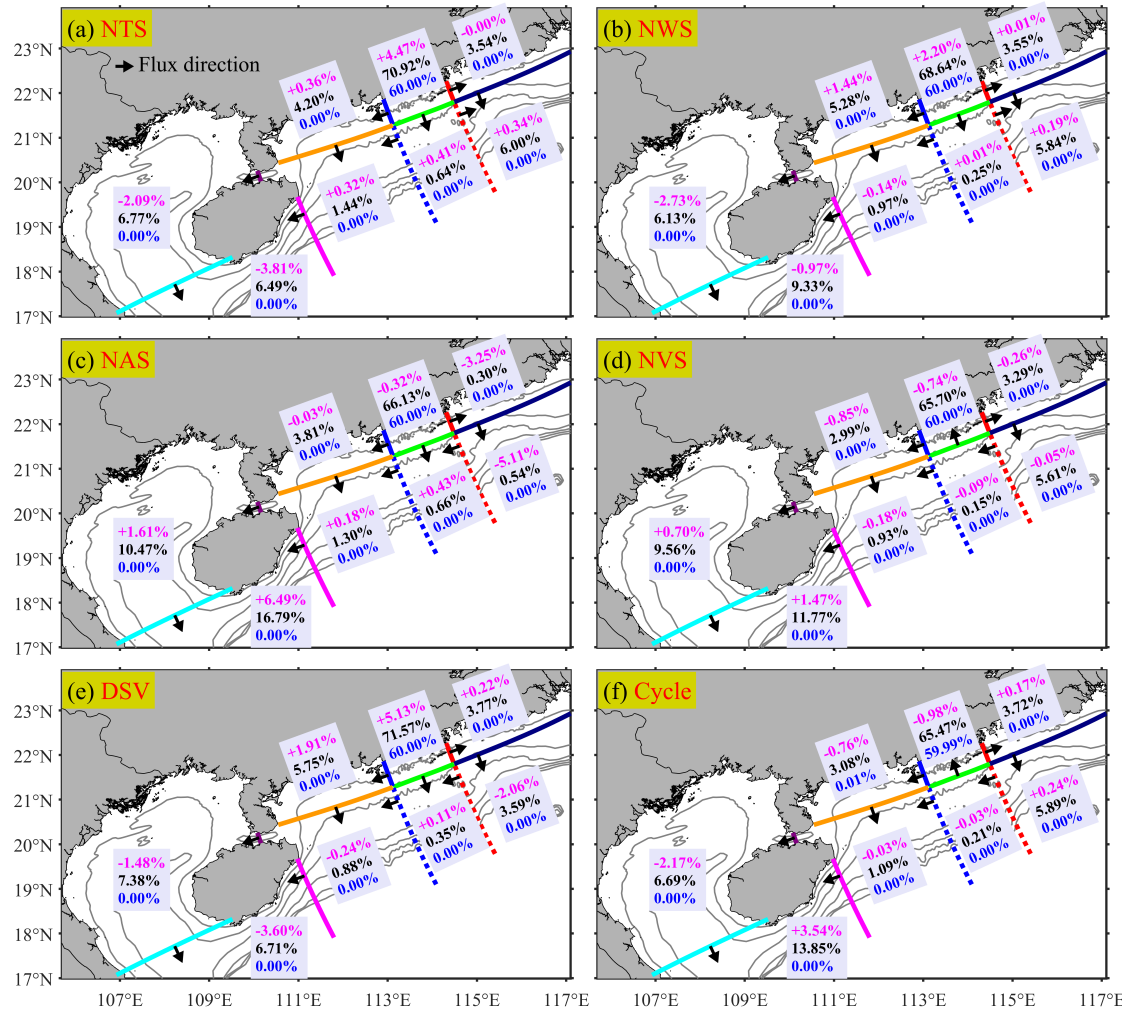


**Figure 12.** Same as Figure 7c, but for the other six cases: (a) NTS, (b) NWS, (c) NAS, (d) NVS, (e) DSV, and (f) Cycle, respectively. All percentages shown in the figure are expressed relative to the annual riverine sediment load (see Figure 3a). Magenta values denote the differences in retention percentage of riverine sediments (Classes 4 and 5; Table 1) between the Control run and each sensitivity case. Black values represent the combined retention of Classes 4 + 5, while blue values indicate Class 5 alone. To obtain the retention percentage for Class 4, simply subtract the Class 5 percentage (blue) from the combined Classes 4 + 5 percentage (black).

## 4. Discussions

### 4.1 Fidelity of our model results

We simulated the suspension, transport, and deposition of the Pearl River-derived sediment over the shelf from April 2017 to March 2018. Comparisons with multiple types of observations demonstrated that the model simulation reasonably well captured the regional patterns and temporal variability of water levels (Figures S2-S4), surface waves (Figures S5-S6), estuarine and shelf currents (Figures S8a-b and S9-S10), salinity and temperature (Figures S7a-b and S8c-d), and SSC (Figures S7c and S8e-f). Even though we have made substantial efforts to collect observational data and conduct calibration and validation, the large scope of the study area and the fact that the study covers an entire year mean that there are some inherent challenges to achieving a complete analysis. The real-world situation may be extremely complex, and these validations may still not be sufficient to address all issues (such as the accurate parameterization of sediment characteristics and their seasonal variations, as well as the proportion of slow-settling fine grains and flocculated flocs in riverine sediments). Therefore, in this section, we intend to discuss the fidelity of our results.

Studies have demonstrated a seasonal dependence of sediment critical shear stress ([Xu et al., 2014](#); [Briggs et al., 2015](#)). On the Louisiana shelf, seabed erodibility is controlled by grain size, sediment age, proximity to river sources, bioturbation, and flood deposits, and is higher during the wet season than the dry season ([Xu et al., 2014](#)). It is also linked to seasonal hypoxia: sites experiencing hypoxic (hypoxia greater than 75% of the time, hypoxia defined as  $< 2 \text{ mg O}_2 \text{ L}^{-1}$ ) conditions exhibit

greater erodibility, whereas the normoxic (hypoxia less than 25% of the time) site shows the lowest erodibility ([Briggs et al., 2015](#)). These findings imply that sediment models should incorporate seasonal variations in critical shear stress, parameterized using field observations or seasonal sampling data. Similarly, in the PRE, field observations, laboratory experiments, and numerical sensitivity analyses have shown that the critical shear stress for erosion of sediments in the PRE is higher in winter/dry season than in summer/wet season ([Dong et al., 2020](#); [Cao et al., 2025](#)). The summer period in the PRE also coincides with seasonal hypoxia ([Cui et al., 2018](#); [Cui et al., 2022](#)), which likely contributes to this seasonal variation in erodibility. Therefore, we considered the seasonal variation of critical shear stress for erosion in a suite of model experiments, that is, increasing the critical shear stress for erosion in winter. This setting was also applied during the 15-month spin-up before conducting the model experiments (the driving force of the spin-up is realistic, i.e., the settings are consistent with those of the Control run). After realistic reworking during the spin-up, the bed sediment grain size distribution (used as initial conditions in the Control run and all Sensitivity cases except the Cycle case) is quite close to the initial prototype (Figures 2d-f vs. 2g-i).

When the seasonal variation of critical shear stress for erosion is omitted (NVS case), the model results suggest a reduced retention of Pearl River-derived sediments in ①–⑥ regions during winter, alongside an increased retention in the "Gulf" and "Distal" regions. However, these differences are relatively small in magnitude compared to the annual load (Figure 12d). Thus, accounting for seasonal variations in

critical shear stress for erosion has a limited influence on the annual-scale retention patterns. The dispersal distance of fluvial sediments on continental shelves is strongly influenced by settling velocity ([Harris et al., 2008](#)). For example, Apennine-derived sediments, characterized by lower settling velocities, travel farther before deposition than Po River sediments, which are predominantly flocculated and settle more rapidly ([Fox et al., 2004](#); [Harris et al., 2008](#)). Likewise, our results suggest that selecting an appropriate settling velocity parameter exerts a greater control on sediment dispersal patterns than accounting for seasonal variations in critical shear stress for erosion (Figure 12d vs. 12e). The results of the DSV case show that a sediment settling velocity twice that of the Control run leads to the highest retention in the "Proximal" and "Western" regions across all experiments (Figure 12e), while reducing the retention in the "Distal" region (Figure 12e). Although the settling velocity we adopted is based on previous studies ([Xia et al., 2004](#)) and model calibrations (Figures S7c and S8e-f), with due consideration given to the presence of slow-settling single fine grains and high-settling flocs in riverine sediments, certain discrepancies might still exist in this setting. These discrepancies are contingent upon the actual magnitude of the low settling velocity of fine grains. In almost all cases, all flocs are retained in the "Proximal" region (Figure 12a-e), and only in the Cycle case, flocs accounting for 0.01% of the annual load are retained in the "Western" region west of the "Proximal" region (Figure 12f, blue values), indicating that high-settling flocs hardly leave the "Proximal" region. This finding shows close alignment with, yet exhibits minor distinctions from, the observed patterns in the Mekong Shelf ([Xue et al., 2012](#)). [Xue](#)

[et al. \(2012\)](#) found that while the preponderance of flocs is deposited on the Mekong delta front precisely at the river mouth, a quantity equivalent to 1.6% of the annual riverine sediment load of flocs is deposited on the downdrift delta front further downstream from the river mouth. This is mainly because the estuarine bay of the PRE is wider and there are numerous islands near the river mouth. The overwhelming majority of flocs are either deposited within the estuarine bay or captured by the surrounding islands. In conclusion, our results are affected by the settling velocity of fine grains. More field observations and studies on model parameterization regarding the settling velocity of fine grains are urgently needed.

As previously noted, we classified riverine sediments into two categories based on established research: 40% slow-settling fine grains and 60% fast-settling flocs. This 40%/60% distribution is consistent with the setting from earlier studies ([Zhang et al., 2019](#); [Zhang et al., 2021](#)), as summarized in Table 1. While such assumptions are necessary for modeling purposes, the actual composition of riverine sediments in natural environments remains uncertain. To evaluate the sensitivity of our results to this uncertainty, we conducted a conceptual analysis. If all riverine sediments were hypothetically composed entirely of fast-settling flocs, they would be completely retained near the source, with no transport to the "Gulf" region. However, this scenario is inconsistent with the radionuclide measurements obtained from "Gulf" region surface sediment samples ([Lin et al., 2020](#)). On the other hand, if all sediments were considered slow-settling fine grains, only 16.13% would be retained in "Proximal" region under normal conditions (or 28.9% in the DSV case), a result that



diverges significantly from established research. [Chen et al. \(2023\)](#) analyzed high-resolution seismic data and demonstrated that approximately 35% of the Pearl River-derived sediment has been transported to offshore shelf areas over the past 6,500 years, suggesting that 65% was deposited proximally. Our findings are in close agreement, indicating that 66.45% of the Pearl River sediments are retained in the proximal region, while 33.55% are transported elsewhere. This consistency with [Chen et al. \(2023\)](#) supports the validity of our approach. Taken together, these analyses confirm that the 40%/60% fraction assumption is a reasonable approximation for modeling purposes.

Furthermore, our model results demonstrate reasonable reliability in other aspects. [Liu et al. \(2009\)](#) and [Ge et al. \(2014\)](#) using chirp sonar profiles from the inner shelf of the South China Sea combined with [Zong et al. \(2009\)](#)'s onshore borehole data, found that the thickness of Pearl River-derived sediments within the PRE since the Holocene is over 20 m, while the mud thickness in the shallow waters west of the Chuanshan Islands (see Figure 1) is approximately 5-10 m. Our calculated annual sediment thicknesses for these two regions are approximately 2 mm and 0.3 mm (Figure 7d), respectively. Given our model's annual riverine sediment load of 34.52 megatons, which has been significantly reduced due to recent human activities ([Dai et al., 2008](#)), compared to the widely accepted Holocene average of around 90 megatons ([Liu et al., 2009](#)), we estimate the total sediment thickness over the past 7500 years to be roughly 39 meters and 6 meters for these depositional zones, consistent with previous studies ([Liu et al., 2009](#); [Zong et al., 2009](#)).

Furthermore, our results reveal that 8.86% of the riverine sediment derived from the Pearl River is transported to the "Gulf" region (Figure 7c), primarily during the winter season (Figure 7b). This finding is not only consistent with the earlier speculation proposed by [Ge et al. \(2014\)](#) but also supplements the conclusions drawn by [Lin et al. \(2020\)](#). From a hydrodynamic perspective, [Shi et al. \(2002\)](#) found that the net flux of currents in the Qiongzhou Strait is westward throughout the year. Our results for both wet summer (Figures 5a-b) and dry winter currents (Figures 6a-b) in the Qiongzhou Strait are consistent with [Shi et al. \(2002\)](#). This westward flow contributes to the westward transport of Pearl River sediment to the "Gulf" region.

## **4.2 Implications of our model results**

The fate of sediment dispersed from the river into the coastal ocean involves at least four processes: supply via buoyant plumes; initial deposition; resuspension and transport by marine processes; and long-term net accumulation ([Wright and Nittrouer, 1995](#)). In general, a significant proportion of river sediment tends to deposit in the estuary and its vicinity ([Walsh and Nittrouer, 2009](#); [Hanebuth et al., 2015](#)).

[Walsh and Nittrouer \(2009\)](#) present a hierarchical decision tree designed to predict the marine dispersal system at a river mouth based on fundamental oceanographic and morphological characteristics. Within this framework, riverine sediment deposition is characterized using key factors, including riverine sediment discharge (greater or less than 2 megatons), shelf width (greater or less than 12 km), and wave and tidal range conditions (greater or less than 2 m) ([Walsh and Nittrouer, 2009](#)).

973 We aim to analyze our PRE simulation results using the framework established  
974 by [Walsh and Nittrouer \(2009\)](#). Although the Pearl River's riverine sediment  
975 discharge (Figure 2a) exceeds the [Walsh and Nittrouer \(2009\)](#)'s 2 megatons per year  
976 threshold, most of the sediment still remains deposited near the estuary (Figure 7c),  
977 indicating an estuarine accumulation-dominated (EAD) system, unlike the  
978 hierarchical decision tree proposed by [Walsh and Nittrouer \(2009\)](#). Outside the estuary,  
979 the continental shelf, spanning 200-220 km in width ([Liu et al., 2014](#)), significantly  
980 exceeds [Walsh and Nittrouer \(2009\)](#)'s 12 km threshold. As a result, most escaped  
981 riverine sediments tend to accumulate on the shelf rather than being captured by  
982 submarine canyons (Figures 7c-d). This wide, shallow shelf promotes sediment  
983 deposition and limits the direct transport of fine sediments into deeper waters ([Walsh](#)  
984 [and Nittrouer, 2009](#)). Subsequently, given that the annual mean tidal range ([Chen et](#)  
985 [al., 2016](#); [Gong et al., 2018b](#)) and Hsig (Figure 3d) near the PRE are both below the 2  
986 m threshold established by [Walsh and Nittrouer \(2009\)](#), the majority of escaped  
987 riverine sediments are predominantly deposited in the proximal depo-center. Our  
988 findings demonstrate that most of our outcomes are consistent with the hierarchical  
989 decision tree proposed by [Walsh and Nittrouer \(2009\)](#), except for the application of  
990 the 2 megatons per year threshold for riverine sediment discharge. This phenomenon  
991 can primarily be attributed to the unique geomorphological characteristics of the PRE,  
992 including its broad mouth (Figures 1 and S1), extensive accommodation space  
993 encompassing approximately 2385 km<sup>2</sup> of water area ([Wu et al., 2018](#)), the presence  
994 and sheltering effect of numerous adjacent islands ([Li et al., 2024b](#)), and the division

of fluvial sediment discharge through eight distinct outlets ([Hu et al., 2011](#)).

The monsoonal nature of the northern SCS (Figures 4a-b) induces pronounced seasonal variations in Pearl River-derived sediment transport and deposition (Figures 5 and 6). During the summer wet season, the Pearl River delivers approximately 95.17% of its annual sediment load to the PRE and the adjacent shelf (Figure 7a) under relatively calm wind and wave conditions (first column of Figure 4), leading to predominant proximal deposition (Figure 5f). In contrast, the winter dry season is characterized by strong northeasterly monsoon winds that generate high-energy waves (second column of Figure 4), significantly increasing bottom shear stress (Figures 4g-h). This process resuspends previously deposited sediments and facilitates their redistribution, particularly toward regions such as the "Gulf" region (Figure 6f).

The PRE exhibits distinctive geomorphological features, yet dispersal of its fine-grained sediment transport on the continental shelf conforms to general patterns observed offshore of other monsoon-influenced estuarine systems. Similar multiple-stage sediment delivery and dispersal mechanisms have been documented offshore of various major estuaries and their adjacent shelves, including the Yellow River Shelf ([Bian et al., 2013](#); [Zeng et al., 2015](#)), Changjiang River Shelf ([Zeng et al., 2015](#)), and Mekong River Shelf ([Xue et al., 2012](#); [Eidam et al., 2017](#)), demonstrating comparable sedimentary processes under monsoon climatic influences. In these systems, sediment transport is not confined to a single process but rather occurs in stages, influenced by seasonal variations in hydrodynamic conditions. Like the PRE Shelf, the Mekong Shelf experiences distinct phases of sediment deposition, with fine

sediments being delivered during periods of high river discharge and then redistributed by waves and tidal forces, particularly during monsoonal shifts ([Xue et al., 2012](#); [Eidam et al., 2017](#)). These complex patterns highlight the interplay between riverine inputs, coastal morphology, and oceanographic processes in shaping sediment dynamics.

These sediment delivery patterns have implications beyond sediment fate, particularly for carbon cycling. Sediment deposition in coastal and shelf areas plays a significant role in trapping organic carbon, influencing long-term carbon burial rates ([LaRowe et al., 2020](#)). Sediment dynamics directly influence the fate of organic carbon (OC) in marine environments, where sediments function as both a sink and a source of OC, playing a pivotal role in global carbon cycling ([Repasch et al., 2021](#)). The multiple-step transport mechanisms can lead to varying carbon storage locations, affecting the sequestration potential of these systems. Additionally, resuspension and redistribution of sediments, especially during high-energy events, may expose previously buried organic material, leading to carbon remineralization and influencing coastal nutrient cycles and ecosystem health ([Ståhlberg et al., 2006](#); [Moriarty et al., 2018](#)). Therefore, understanding these patterns is crucial for assessing the broader impacts on carbon cycling and coastal biogeochemical processes.

### **4.3 Limitations and future work**

This study focuses on analyzing simulation results from a typical year, encompassing both wet and dry seasons from 2017 to 2018, to understand the seasonal variations and annual patterns of suspension, transport, and deposition of

sediment in the PRE and adjacent shelf. However, it's essential to recognize that the long-term sediment transport and deposition dynamics in the Pearl River are influenced by numerous complex factors. These include changes in sea level and coastal line ([Church and White, 2006](#); [Harff et al., 2010](#); [Hong et al., 2020](#); [Lin et al., 2022](#); [Ma et al., 2023](#)), alterations in wind field and precipitation ([Ning and Qian, 2009](#); [Young et al., 2011](#)), natural sedimentation within the Pearl River Delta ([Wu et al., 2010](#)), modifications in sediment load and underwater volume of the estuary caused by anthropogenic impact ([Wu et al., 2014](#); [Wu et al., 2018](#); [Lin et al., 2022](#)), interannual variations of the shelf circulations ([Liu et al., 2020](#); [Deng et al., 2022](#)) and Kuroshio intrusions ([Caruso et al., 2006](#); [Nan et al., 2015](#); [Sun et al., 2020](#)). Therefore, while this study sheds light on seasonal and annual timescale patterns, it cannot fully represent the short or long-term transport and deposition trends of the Pearl River sediment. Yet for many shelf systems, a lot of sediment transport happens during short-lived events such as hurricanes ([Xu et al., 2016](#); [Warner et al., 2017](#); [Georgiou et al., 2024](#)). Consideration of the episodicity of transport would be helpful for future studies ([Xu et al., 2016](#); [Warner et al., 2017](#); [Georgiou et al., 2024](#)).

Additionally, it's important to note that this article primarily focuses on the fate of the Pearl River sediment on the inner shelf. However, within the expansion range of the Pearl River buoyant plume, a number of smaller rivers, including the Jiulong River, Han River, Moyang River, Jian River, Nanliu River, Changhua River and Nandu River, also contribute freshwater and sediment to the northern South China Sea ([Milliman and Farnsworth, 2011](#); [Zhang et al., 2012](#); [Liu et al., 2016](#)). Although these

rivers contribute significantly less freshwater and sediment compared to the Pearl River, they still impact seawater salinity, suspended sediment concentration, and seabed geomorphology ([Liu et al., 2016](#); [Wang et al., 2023](#); [Zong et al., 2024](#)). Since the 1950s, South China delivers approximately 102 Mt/year of fluvial sediment to the SCS, with the Pearl River alone accounting for 84.3 Mt/year—about 83% of the total sediment load ([Milliman and Farnsworth, 2011](#); [Zhang et al., 2012](#); [Liu et al., 2016](#)). The specific contributions of each river are detailed in Table 3. While the data highlight the Pearl River's dominant role in sediment delivery, a comprehensive understanding of sedimentary processes and impacts in the northern South China Sea also requires systematic investigation into the roles of the smaller contributing rivers.

**Table 3.** Annual mean runoff and annual suspended sediment load of major rivers in South China that flow directly into the northern South China Sea since the 1950s ([Milliman and Farnsworth, 2011](#); [Zhang et al., 2012](#); [Liu et al., 2016](#)).

River name	Runoff (m <sup>3</sup> s <sup>-1</sup> )	Suspended sediment load (Mt/year)
Pearl River	9075	84.3
Jiulong River	476	3.1
Han River	825	10
Moyang River	269	0.8
Jian River	174	1.5
Nanliu River	162	1.1
Changhua River	120	0.08

Nandu River	179	0.4
-------------	-----	-----

1075

1076        Then, while the model used in this study has shown good validation results,  
1077 conducting more sensitivity experiments on sediment parameters, such as settling  
1078 velocity and critical shear stress for erosion, would be beneficial. Settling velocity can  
1079 influence the location of sediment depocenters, with higher settling velocities leading  
1080 to more proximal entrapment and vice versa ([Harris et al., 2008](#)). Similarly, critical  
1081 erosion stress can affect the resuspension of deposited sediment, with higher critical  
1082 erosion stress resulting in less resuspension and more deposition especially during  
1083 neap tides and weak wind wave events ([Dong et al., 2020](#); [Choi et al., 2023](#)).  
1084 Conducting such sensitivity analyses would enhance our understanding of sediment  
1085 dynamics in estuaries and shelves. Besides, the model does not account for cohesive  
1086 processes, such as consolidation and flocculation, which can significantly impact  
1087 sediment behavior ([Sherwood et al., 2018](#)). Our model does not incorporate wave and  
1088 current-supported gravity flows, which are important factors influencing sediment  
1089 transport in submarine canyon areas ([Harris et al., 2005](#); [Ma et al., 2010](#); [Zhang et al.,](#)  
1090 [2020](#)). Since our study area primarily focuses on the continental shelf and the  
1091 simulated results indicate that sediment transport occurs mainly in the shallow inner  
1092 shelf, where canyons are relatively rare, this omission has a relatively minor impact  
1093 on our results.

1094        Lastly, we employ the COAWST model, which uses an S-coordinate system in  
1095 the vertical direction with increased resolution near the surface and bottom layers



([Song and Haidvogel, 1994](#)). This vertical layering allows cell heights to vary, enabling finer resolution in dynamically important regions and improving performance in areas with sloping bathymetry compared to traditional sigma-coordinate systems ([Bryan, 1969](#); [Song and Haidvogel, 1994](#)). In addition, our model includes horizontal grid refinement in the PRE, enhancing its ability to resolve estuarine features. As a result, the model effectively captures estuarine turbidity maxima (ETM) and horizontal salinity fronts (Figures S11 and S12, see Supplement). During summer, multiple ETMs appear near the estuary bottom (Figure S11b), and while these features persist in winter, their concentrations vary (Figure S12b), consistent with the findings of [Wang et al. \(2018\)](#), [Zhan et al. \(2019\)](#), [Zhang et al. \(2021\)](#), [Ma et al. \(2022\)](#), and [Ma et al. \(2024\)](#). Horizontal salinity fronts are also well represented, showing an upstream shift from the high-discharge summer season to the low-discharge winter season (Figures S11e–f and S12e–f), in agreement with previous studies by [Zhang et al. \(2021\)](#) and [Ma et al. \(2024\)](#). Nonetheless, compared with the S-coordinate system, models that employ vertically adaptive layering (e.g., SCHISM, the Semi-implicit Cross-scale Hydroscience Integrated System Model, [Zhang et al. \(2016\)](#)) or Cartesian vertical coordinates (e.g., MITgcm, the MIT General Circulation Model, [Marshall et al. \(1997a\)](#); [Marshall et al. \(1997b\)](#)) generally perform better in regions with steep topographic gradients ([Bijvelds, 2001](#)). Therefore, future research could benefit from adopting models with higher horizontal resolution and Cartesian vertical coordinates to improve the simulation of Pearl River-derived sediment dynamics across the estuary and the adjacent shelf.

1118

## 1119 **5. Conclusions**

1120 This study utilizes the COAWST model to quantitatively analyze the seasonal  
1121 suspension, transport, and annual fate of Pearl River-derived sediment (classes 4-5 in  
1122 Table 1) on the continental shelf over a typical year, capturing key marine variables  
1123 such as water level, wave height, flow velocity, salinity, temperature, and SSC.

1124 The monsoonal nature of the northern SCS (Figures 4a-b) induces pronounced  
1125 seasonal variations in Pearl River-derived sediment transport and deposition (Figures  
1126 5 and 6). During the wet summer, calm conditions foster initial Pearl River-derived  
1127 sediment deposition via the buoyant plume (Figures 5 and 7a). Conversely, winter's  
1128 stronger winds and waves resuspend and transport Pearl River-derived sediments into  
1129 "Gulf" region (Figures 6 and 7b). Our quantitative assessment reveals distinct spatial  
1130 patterns in the annual fate of riverine sediments: approximately two-thirds of the Pearl  
1131 River-derived sediment is retained within the estuarine vicinity ("Proximal" region),  
1132 while about 9% reaches the continental shelf east of the PRE ("Eastern" and  
1133 "Southeastern" regions), while similar proportions are transported to and retained in  
1134 "Gulf" and "Distal" regions, respectively (Figure 7c). Furthermore, we evaluated the  
1135 contributions of different physical processes by comparing the Control run with the  
1136 reduced-physics sensitivity experiments. Our analysis reveals distinct roles of tidal  
1137 forces, wave action, and background circulation in governing the transport and  
1138 deposition of Pearl River-derived sediments (Figures 8, 9, 11a-c, and 12a-c).

1139 Tidal dynamics primarily govern sediment behavior within and offshore of the

1140 PRE. Relative to the Control run, neglecting tides leads to lower bottom shear stress  
1141 in the PRE (Figures 8a-b), higher Pearl River-derived sediment deposition in the PRE  
1142 (Figure 11a), and reduced sediment retention in “Gulf” and “Distal” regions (Figure  
1143 12a). Wave activity primarily controls Pearl River-derived sediment resuspension in  
1144 three critical dimensions: (1) the river mouth, (2) the nearshore of "Eastern" and  
1145 "Western" regions outside the estuary, and (3) periods characterized by high wave  
1146 energy during winter (Figures 9c-d). Excluding waves results in increased modeled  
1147 Pearl River-derived sediment deposition in these areas and times (Figure 11b), while  
1148 reducing accumulation in the "Gulf" region (Figure 11b). Background circulation is  
1149 most influential in summer (Figure 5a vs. Figure 9e), with a strong northeastward  
1150 current transporting Pearl River-derived sediments to regions ③–④. Without this  
1151 current and under weak southerly winds, only 0.84% of Pearl River-derived sediments  
1152 are transported to regions ③–④, while deposition in “Gulf” and “Distal” regions is  
1153 greater compared to the Control run (Figure 12c). The sediment model solutions are  
1154 also highly sensitive to the parameterization of sediment characteristics and spin-up  
1155 durations (riverine or seabed sediments) (Figures 10, 11d-f, and 12d-f). Neglecting the  
1156 seasonal increase in critical shear stress for erosion leads to enhanced resuspension  
1157 and erosion in regions ①–⑥ during winter (Figure 10b), which in turn shifts more  
1158 sediment toward “Gulf” and “Distal” regions compared to the Control run (Figure  
1159 12d). Increasing the settling velocity reduces the overall riverine SSC (Figures 10c-d)  
1160 and results in a spatial redistribution pattern characterized by greater retention in ①–  
1161 ③ and ⑤ regions and reduced riverine sediment presence in “Gulf” and “Distal”

regions relative to the Control simulation (Figure 12e). Additionally, the modeled riverine SSC is influenced by pre-existing Pearl River–derived sediments, as shown in the Cycle experiment (Figure 10e-f). The experiment highlights the effect of riverine sediment spin-up, showing that first-year retained Pearl River–derived sediments are predominantly redistributed from the “Gulf” region toward the more distant “Distal” region during the second year. In contrast, the model exhibits only minor sensitivity to the duration of seabed sediment spin-up, as demonstrated in the Cycle2 experiment (see Supplement), in which riverine sediments present during the spin-up period were added to seabed sediment classes 1–2 at the start of the Cycle2.

## **Acknowledgments**

This research was funded by the National Natural Science Foundation of China (grant numbers 42306015 and 42276169), the China Postdoctoral Science Foundation (grant number 2023M743988). Wenping Gong is supported by the Southern Marine Science and Engineering Guangdong Laboratory (Zhuhai) (SML2023SP238). The authors would like to thank the crew of the R/V Changhe Ocean for their valuable contribution during the collection of the field data. We express our gratitude to the Co-editors-in-chief, Dr. Mario Hoppema, and three anonymous reviewers for their valuable suggestions in enhancing and improving this article.

## **Data availability**

The HYbrid Coordinate Ocean Model (HYCOM) outputs are from: <http://hycom.org/hycom>. The NCEP Climate Forecast System Version 2 (CFSv2) reanalysis data can be obtained at the following website:

<https://rda.ucar.edu/datasets/ds094.1/dataaccess/>. The NOAA WAVEWATCH III global ocean wave model output fields can be downloaded from: <ftp://polar.ncep.noaa.gov/pub/history/waves>. Hourly water-level data observed at Quarry Bay station are provided by the Hong Kong Observatory website: <https://www.hko.gov.hk/sc/tide/marine/realtide.htm?s=QUB&t=TABLE>. Hourly water-level data from Zhapo and Qinglan stations, provided by the Flanders Marine Institute (VLIZ), are part of the UNESCO/IOC Global Sea Level Observing System (GLOSS) and accessible at <http://www.ioc-sealevelmonitoring.org>. The mooring data for the M1 and M2 stations are sourced from [Liu et al. \(2023\)](#) and [Li et al. \(2024a\)](#). The figure data and model configuration files used in this paper can be downloaded from: <https://doi.org/10.5281/zenodo.15013448>.

## **Declaration of Competing interests**

The authors declare that they have no known competing financial interests or personal relationships that could have appeared to influence the work reported in this paper.

## **CRedit authorship contribution statement**

**GZ:** Conceptualization, Numerical modeling, Validation, Data visualization, Writing-original draft, and Funding acquisition. **SH:** Writing-review & editing, Validation. **XY:** Writing-review & editing. **HZ:** Writing-review & editing. **WG:** Writing-review & editing, and Funding acquisition

## **Supplement:**

The Supplement includes validation and analysis of the model's water levels,

Hsig, flow velocities, salinity, temperature, and SSC. It provides additional text and figures that support the model validation and supplementary analyses, which could not be fully presented in the main article due to space limitations.

## References

- Bever, A. J., Harris, C. K., Sherwood, C. R., and Signell, R. P.: Deposition and flux of sediment from the Po River, Italy: An idealized and wintertime numerical modeling study, *Marine Geology*, 260, 69-80, 10.1016/j.margeo.2009.01.007, 2009.
- Bever, A. J., and MacWilliams, M. L.: Simulating sediment transport processes in San Pablo Bay using coupled hydrodynamic, wave, and sediment transport models, *Marine Geology*, 345, 235-253, 10.1016/j.margeo.2013.06.012, 2013.
- Bian, C., Jiang, W., and Greatbatch, R. J.: An exploratory model study of sediment transport sources and deposits in the Bohai Sea, Yellow Sea, and East China Sea, *Journal of Geophysical Research: Oceans*, 118, 5908-5923, <https://doi.org/10.1002/2013JC009116>, 2013.
- Bijvelds, M. D. J. P.: Numerical modelling of estuarine flow over steep topography, Doctoral, Delft University of Technology, 2001.
- Booij, N., Ris, R. C., and Holthuijsen, L. H.: A third-generation wave model for coastal regions: 1. Model description and validation, *Journal of Geophysical Research: Oceans*, 104, 7649-7666, <https://doi.org/10.1029/98JC02622>, 1999.
- Brand, A., Lacy, J. R., Hsu, K., Hoover, D., Gladding, S., and Stacey, M. T.: Wind-enhanced resuspension in the shallow waters of South San Francisco Bay: Mechanisms and potential implications for cohesive sediment transport, *Journal of Geophysical Research*, 115, 10.1029/2010jc006172, 2010.
- Briggs, K. B., Cartwright, G., Friedrichs, C. T., and Shivarudruppa, S.: Biogenic effects on cohesive sediment erodibility resulting from recurring seasonal hypoxia on the Louisiana shelf, *Continental Shelf Research*, 93, 17-26, <https://doi.org/10.1016/j.csr.2014.11.005>, 2015.
- Bryan, K.: A numerical method for the study of the circulation of the world ocean, *Journal of Computational Physics*, 4, 347-376, [https://doi.org/10.1016/0021-9991\(69\)90004-7](https://doi.org/10.1016/0021-9991(69)90004-7), 1969.
- Burchard, H., Schuttelaars, H. M., and Ralston, D. K.: Sediment Trapping in Estuaries, *Annual Review*

1234 of Marine Science, 10, 371-395, 10.1146/annurev-marine-010816-060535, 2018.

1235 Cao, L., Liu, J., Shi, X., He, W., and Chen, Z.: Source-to-sink processes of fluvial sediments in the  
 1236 northern South China Sea: Constraints from river sediments in the coastal region of South China,  
 1237 Journal of Asian Earth Sciences, 185, 104020, 10.1016/j.jseaes.2019.104020, 2019.

1238 Cao, Z., Ren, J., Deng, Z., Ye, L., and Wu, J.: Small-scale spatial variability in erosion threshold and  
 1239 bedform for cohesive sediment measured by 3D Sonar, Journal of Hydrology, 650, 132513,  
 1240 10.1016/j.jhydrol.2024.132513, 2025.

1241 Caruso, M. J., Gawarkiewicz, G. G., and Beardsley, R. C.: Interannual variability of the Kuroshio  
 1242 intrusion in the South China Sea, Journal of Oceanography, 62, 559-575,  
 1243 10.1007/s10872-006-0076-0, 2006.

1244 Chapman, D. C.: Numerical Treatment of Cross-Shelf Open Boundaries in a Barotropic Coastal Ocean  
 1245 Model, Journal of Physical Oceanography, 15, 1060-1075, 1985.

1246 Charnock, H.: Wind stress on a water surface, Quarterly Journal of the Royal Meteorological Society,  
 1247 81, 639-640, <https://doi.org/10.1002/qj.49708135027>, 1955.

1248 Chassignet, E. P., Hurlburt, H. E., Smedstad, O. M., Halliwell, G. R., Hogan, P. J., Wallcraft, A. J.,  
 1249 Baraille, R., and Bleck, R.: The HYCOM (HYbrid Coordinate Ocean Model) data assimilative  
 1250 system, Journal of Marine Systems, 65, 60-83, <https://doi.org/10.1016/j.jmarsys.2005.09.016>,  
 1251 2007.

1252 Chen, S.-N., Geyer, W. R., Sherwood, C. R., and Ralston, D. K.: Sediment transport and deposition on  
 1253 a river-dominated tidal flat: An idealized model study, Journal of Geophysical Research, 115,  
 1254 10.1029/2010jc006248, 2010.

1255 Chen, Y., Deng, B., Saito, Y., Wang, Z., Yang, X., and Wu, J.: Pearl River sediment dispersal over its  
 1256 associated delta–estuary–shelf system during the Holocene, Sedimentology, 70, 2331-2354,  
 1257 10.1111/sed.13123, 2023.

1258 Chen, Z., Pan, J., and Jiang, Y.: Role of pulsed winds on detachment of low salinity water from the  
 1259 Pearl River Plume Upwelling and mixing processes, Journal of Geophysical Research: Oceans,  
 1260 121, 2769-2788, 10.1002/2015JC011337, 2016.

1261 Chen, Z., Gong, W., Cai, H., Chen, Y., and Zhang, H.: Dispersal of the Pearl River plume over  
 1262 continental shelf in summer, Estuarine, Coastal and Shelf Science, 194, 252-262,

10.1016/j.ecss.2017.06.025, 2017a.

Chen, Z., Pan, J., Jiang, Y., and Lin, H.: Far-reaching transport of Pearl River plume water by upwelling jet in the northeastern South China Sea, *Journal of Marine Systems*, 173, 60-69, 10.1016/j.jmarsys.2017.04.008, 2017b.

Cheng, P., Li, M., and Li, Y.: Generation of an estuarine sediment plume by a tropical storm, *Journal of Geophysical Research: Oceans*, 118, 856-868, 10.1002/jgrc.20070, 2013.

Choi, S. M., Seo, J. Y., and Ha, H. K.: Contribution of local erosion enhanced by winds to sediment transport in intertidal flat, *Marine Geology*, 465, 107171, 10.1016/j.margeo.2023.107171, 2023.

Church, J. A., and White, N. J.: A 20th century acceleration in global sea-level rise, *Geophysical Research Letters*, 33, n/a-n/a, 10.1029/2005gl024826, 2006.

Cui, Y., Wu, J., Ren, J., and Xu, J.: Physical dynamics structures and oxygen budget of summer hypoxia in the Pearl River Estuary, *Limnology and Oceanography*, 64, 131-148, 10.1002/lno.11025, 2018.

Cui, Y., Wu, J., Tan, E., and Kao, S. J.: Role of Particle Resuspension in Maintaining Hypoxic Level in the Pearl River Estuary, *Journal of Geophysical Research: Oceans*, 127, 10.1029/2021jc018166, 2022.

Dai, S. B., Yang, S. L., and Cai, A. M.: Impacts of dams on the sediment flux of the Pearl River, southern China, *Catena*, 76, 36-43, 10.1016/j.catena.2008.08.004, 2008.

Dalyander, P. S., Butman, B., Sherwood, C. R., Signell, R. P., and Wilkin, J. L.: Characterizing wave- and current- induced bottom shear stress: U.S. middle Atlantic continental shelf, *Continental Shelf Research*, 52, 73-86, <https://doi.org/10.1016/j.csr.2012.10.012>, 2013.

Deng, Y., Liu, Z., Zu, T., Hu, J., Gan, J., Lin, Y., Li, Z., Quan, Q., and Cai, Z.: Climatic Controls on the Interannual Variability of Shelf Circulation in the Northern South China Sea, *Journal of Geophysical Research: Oceans*, 127, e2022JC018419, <https://doi.org/10.1029/2022JC018419>, 2022.

Dong, H., Jia, L., He, Z., Yu, M., and Shi, Y.: Application of parameters and paradigms of the erosion and deposition for cohesive sediment transport modelling in the Lingdingyang Estuary, China, *Applied Ocean Research*, 94, 101999, 10.1016/j.apor.2019.101999, 2020.

Dong, L., Su, J., Wong, L., Cao, Z., and Chen, J.: Seasonal variation and dynamics of the Pearl River



1292 plume, *Continental Shelf Research*, 24, 1761-1777, 10.1016/j.csr.2004.06.006, 2004.

1293 Egbert, G. D., and Erofeeva, S. Y.: Efficient inverse Modeling of barotropic ocean tides, *Journal of*  
1294 *Atmospheric and Oceanic Technology*, 19, 183-204, Doi  
1295 10.1175/1520-0426(2002)019<0183:Eimobo>2.0.Co;2, 2002.

1296 Eidam, E. F., Nittrouer, C. A., Ogston, A. S., DeMaster, D. J., Liu, J. P., Nguyen, T. T., and Nguyen, T.  
1297 N.: Dynamic controls on shallow clinoform geometry: Mekong Delta, Vietnam, *Continental Shelf*  
1298 *Research*, 147, 165-181, 10.1016/j.csr.2017.06.001, 2017.

1299 Fairall, C. W., Bradley, E. F., Rogers, D. P., Edson, J. B., and Young, G. S.: Bulk parameterization of  
1300 air-sea fluxes for Tropical Ocean-Global Atmosphere Coupled-Ocean Atmosphere Response  
1301 Experiment, *Journal of Geophysical Research: Oceans*, 101, 3747-3764,  
1302 <https://doi.org/10.1029/95JC03205>, 1996.

1303 Flather, R. A.: A tidal model of the north-west European continental shelf, *Memoires Societe Royale*  
1304 *des Sciences de Liege*, 10, 141-164, 1976.

1305 Fox, J. M., Hill, P. S., Milligan, T. G., Ogston, A. S., and Boldrin, A.: Flocculation in the waters of the  
1306 Po River prodelta, *Continental Shelf Research*, 24, 1699-1715,  
1307 <https://doi.org/10.1016/j.csr.2004.05.009>, 2004.

1308 Gan, J., Cheung, A., Guo, X., and Li, L.: Intensified upwelling over a widened shelf in the northeastern  
1309 South China Sea, *Journal of Geophysical Research*, 114, 10.1029/2007jc004660, 2009.

1310 Gan, J., San Ho, H., and Liang, L.: Dynamics of Intensified Downwelling Circulation over a Widened  
1311 Shelf in the Northeastern South China Sea, *Journal of Physical Oceanography*, 43, 80-94,  
1312 10.1175/jpo-d-12-02.1, 2013.

1313 Gao, S., and Collins, M. B.: Holocene sedimentary systems on continental shelves, *Marine Geology*,  
1314 352, 268-294, 10.1016/j.margeo.2014.03.021, 2014.

1315 Gao, X., Chen, S., Xie, X., Long, A., and Ma, F.: Non-aromatic hydrocarbons in surface sediments near  
1316 the Pearl River estuary in the South China Sea, *Environmental Pollution*, 148, 40-47,  
1317 10.1016/j.envpol.2006.11.001, 2007.

1318 Gao, X., Arthur Chen, C.-T., Wang, G., Xue, Q., Tang, C., and Chen, S.: Environmental status of Daya  
1319 Bay surface sediments inferred from a sequential extraction technique, *Estuarine, Coastal and*  
1320 *Shelf Science*, 86, 369-378, 10.1016/j.ecss.2009.10.012, 2010.

1321 Ge, Q., Liu, J. P., Xue, Z., and Chu, F.: Dispersal of the Zhujiang River (Pearl River) derived sediment  
 1322 in the Holocene, *Acta Oceanologica Sinica*, 33, 1-9, 10.1007/s13131-014-0407-8, 2014.

1323 Ge, Q., Xue, Z., Yao, Z., Zang, Z., and Chu, F.: Anti-phase relationship between the East Asian winter  
 1324 monsoon and summer monsoon during the Holocene?, *Journal of Ocean University of China*, 16,  
 1325 175-183, 10.1007/s11802-017-3098-x, 2017.

1326 Ge, Q., Xu, D., Ye, L., Yang, K., and Yao, Z.: Linking Monsoon Activity with River-Derived Sediments  
 1327 Deposition in the Northern South China Sea, *Journal of Ocean University of China*, 18, 1098-1104,  
 1328 10.1007/s11802-019-4155-4, 2019.

1329 Georgiou, I. Y., FitzGerald, D. M., Sakib, M. M., Messina, F., Kulp, M. A., and Miner, M. D.: Storm  
 1330 Dynamics Control Sedimentation and Shelf-Bay-Marsh Sediment Exchange Along the Louisiana  
 1331 Coast, *Geophysical Research Letters*, 51, e2024GL111344,  
 1332 <https://doi.org/10.1029/2024GL111344>, 2024.

1333 Geyer, W. R., Hill, P. S., and Kineke, G. C.: The transport, transformation and dispersal of sediment by  
 1334 buoyant coastal flows, *Continental Shelf Research*, 24, 927-949, 10.1016/j.csr.2004.02.006, 2004.

1335 Gong, W., Chen, Y., Zhang, H., and Chen, Z.: Effects of Wave–Current Interaction on Salt Intrusion  
 1336 During a Typhoon Event in a Highly Stratified Estuary, *Estuaries and Coasts*, 41, 1904-1923,  
 1337 10.1007/s12237-018-0393-8, 2018a.

1338 Gong, W., Lin, Z., Chen, Y., Chen, Z., Shen, J., and Zhang, H.: Effect of waves on the dispersal of the  
 1339 Pearl River plume in winter, *Journal of Marine Systems*, 186, 47-67,  
 1340 10.1016/j.jmarsys.2018.05.003, 2018b.

1341 Haidvogel, D. B., Arango, H., Budgell, W. P., Cornuelle, B. D., Curchitser, E., Di, L. E., Fennel, K.,  
 1342 Geyer, W. R., Hermann, A. J., Lanerolle, L., Levin, J., McWilliams, J. C., Miller, A. J., Moore, A.  
 1343 M., Powell, T. M., Shchepetkin, A. F., Sherwood, C. R., Signell, R. P., Warner, J. C., and Wilkin, J.:  
 1344 Ocean forecasting in terrain-following coordinates: Formulation and skill assessment of the  
 1345 Regional Ocean Modeling System, *Journal of Computational Physics*, 227, 3595-3624,  
 1346 10.1016/j.jcp.2007.06.016, 2008.

1347 Hanebuth, T. J. J., Lantzsch, H., and Nizou, J.: Mud depocenters on continental shelves—appearance,  
 1348 initiation times, and growth dynamics, *Geo-Marine Letters*, 35, 487-503,  
 1349 10.1007/s00367-015-0422-6, 2015.

1350 Harff, J., Leipe, T., and Zhou, D.: Pearl River Estuary related sediments as response to Holocene  
1351 climate change and anthropogenic impact (PECAI), *Journal of Marine Systems*, 82, S1-S2,  
1352 10.1016/j.jmarsys.2010.02.008, 2010.

1353 Harris, C. K., Traykovski, P. A., and Geyer, W. R.: Flood dispersal and deposition by near-bed  
1354 gravitational sediment flows and oceanographic transport: A numerical modeling study of the Eel  
1355 River shelf, northern California, *Journal of Geophysical Research: Oceans*, 110,  
1356 10.1029/2004jc002727, 2005.

1357 Harris, C. K., Sherwood, C. R., Signell, R. P., Bever, A. J., and Warner, J. C.: Sediment dispersal in the  
1358 northwestern Adriatic Sea, *Journal of Geophysical Research*, 113, 10.1029/2006jc003868, 2008.

1359 Hong, B., Liu, Z., Shen, J., Wu, H., Gong, W., Xu, H., and Wang, D.: Potential physical impacts of  
1360 sea-level rise on the Pearl River Estuary, China, *Journal of Marine Systems*, 201, 103245,  
1361 10.1016/j.jmarsys.2019.103245, 2020.

1362 Hu, J., Li, S., and Geng, B.: Modeling the mass flux budgets of water and suspended sediments for the  
1363 river network and estuary in the Pearl River Delta, China, *Journal of Marine Systems*, 88, 252-266,  
1364 10.1016/j.jmarsys.2011.05.002, 2011.

1365 Hu, S., Li, Y., Hu, P., Zhang, H., Zhang, G., and Gong, W.: The Impacts of Far-Field Typhoon-  
1366 Generated Coastal Trapped Waves on the Hydrodynamics in the Northern South China Sea: A  
1367 Case Study of Typhoon In - Fa, *Journal of Geophysical Research: Oceans*, 129,  
1368 10.1029/2024jc021359, 2024.

1369 Huang, D., Du, J., Deng, B., and Zhang, J.: Distribution patterns of particle-reactive radionuclides in  
1370 sediments off eastern Hainan Island, China: Implications for source and transport pathways,  
1371 *Continental Shelf Research*, 57, 10-17, 10.1016/j.csr.2012.04.019, 2013.

1372 Jacob, R., Larson, J., and Ong, E.:  $M \times N$  Communication and Parallel Interpolation in Community  
1373 Climate System Model Version 3 Using the Model Coupling Toolkit, *IJHPCA*, 19, 293-307,  
1374 10.1177/1094342005056116, 2005.

1375 Kirby, M. F., Devoy, B., Law, R. J., Ward, A., and Aldridge, J.: The use of a bioassay based approach to  
1376 the hazard/risk assessment of cargo derived toxicity during shipping accidents: a case study--the  
1377 MSC Napoli, *Marine Pollution Bulletin*, 56, 781-786, 10.1016/j.marpolbul.2008.01.006, 2008.

1378 Krige, D. G.: A Statistical Approach to Some Basic Mine Valuation Problems on the Witwatersrand,  
 1379 Chemical, Metallurgical and Mining Society of South Africa, 1951.

1380 Kuehl, S. A., Alexander, C. R., Blair, N. E., Harris, C. K., Marsaglia, K. M., Ogston, A. S., Orpin, A. R.,  
 1381 Roering, J. J., Bever, A. J., Bilderback, E. L., Carter, L., Cerovski-Darriau, C., Childress, L. B.,  
 1382 Reide Corbett, D., Hale, R. P., Leithold, E. L., Litchfield, N., Moriarty, J. M., Page, M. J., Pierce,  
 1383 L. E. R., Upton, P., and Walsh, J. P.: A source-to-sink perspective of the Waipaoa River margin,  
 1384 Earth-Science Reviews, 153, 301-334, 10.1016/j.earscirev.2015.10.001, 2016.

1385 Kumar, N., Voulgaris, G., Warner, J. C., and Olabarrieta, M.: Implementation of the vortex force  
 1386 formalism in the coupled ocean-atmosphere-wave-sediment transport (COAWST) modeling  
 1387 system for inner shelf and surf zone applications, Ocean Modelling, 47, 65-95,  
 1388 10.1016/j.ocemod.2012.01.003, 2012.

1389 LaRowe, D. E., Arndt, S., Bradley, J. A., Estes, E. R., Hoarfrost, A., Lang, S. Q., Lloyd, K. G.,  
 1390 Mahmoudi, N., Orsi, W. D., Shah Walter, S. R., Steen, A. D., and Zhao, R.: The fate of organic  
 1391 carbon in marine sediments - New insights from recent data and analysis, Earth-Science Reviews,  
 1392 204, 103146, 10.1016/j.earscirev.2020.103146, 2020.

1393 Larson, J., Jacob, R., and Ong, E.: The Model Coupling Toolkit: A New Fortran90 Toolkit for Building  
 1394 Multiphysics Parallel Coupled Models, IJHPCA, 19, 277-292, 2005.

1395 Li, J., Li, M., and Xie, L.: Observations of near-inertial oscillations trapped at inclined front on  
 1396 continental shelf of the northwestern South China Sea, EGU sphere, 2024, 1-25,  
 1397 10.5194/egusphere-2024-3909, 2024a.

1398 Li, X., Chrysagi, E., Klingbeil, K., and Burchard, H.: Impact of Islands on Tidally Dominated River  
 1399 Plumes: A High-Resolution Modeling Study, Journal of Geophysical Research: Oceans, 129,  
 1400 e2023JC020272, <https://doi.org/10.1029/2023JC020272>, 2024b.

1401 Lin, S., Niu, J., Liu, G., Wei, X., and Cai, S.: Variations of suspended sediment transport caused by  
 1402 changes in shoreline and bathymetry in the Zhujiang (Pearl) River Estuary in the wet season, Acta  
 1403 Oceanologica Sinica, 41, 54-73, 10.1007/s13131-022-2017-1, 2022.

1404 Lin, W., Feng, Y., Yu, K., Lan, W., Wang, Y., Mo, Z., Ning, Q., Feng, L., He, X., and Huang, Y.:  
 1405 Long-lived radionuclides in marine sediments from the Beibu Gulf, South China Sea: Spatial  
 1406 distribution, controlling factors, and proxy for transport pathway, Marine Geology, 424, 106157,

10.1016/j.margeo.2020.106157, 2020.

Liu, G., and Cai, S.: Modeling of suspended sediment by coupled wave-current model in the Zhujiang (Pearl) River Estuary, *Acta Oceanologica Sinica*, 38, 22-35, 10.1007/s13131-019-1455-3, 2019.

Liu, H., Ye, L., Zhou, W., and Wu, J.: Salt-wedge intrusion-retreat cycle induced sediment flocculation dynamics in bottom boundary layer (BBL) of a micro-tidal estuary, *Marine Geology*, 466, 107175, 10.1016/j.margeo.2023.107175, 2023.

Liu, J. P., Xue, Z., Ross, K., Yang, Z., and Gao, S.: Fate of Sediments Delivered to the Sea by Asian Large Rivers: Long-Distance Transport and Formation of Remote Alongshore Clinothems, *Sediment. Rec.*, 7, 10.2110/sedred.2009.4.4, 2009.

Liu, N., Geng, B., Xue, H., Xiu, P., Wang, Q., and Wang, D.: Interannual Variability of Shelf and Slope Circulations in the Northern South China Sea, *Journal of Ocean University of China*, 19, 1005-1016, 10.1007/s11802-020-4446-9, 2020.

Liu, Y., Gao, S., Wang, Y. P., Yang, Y., Long, J., Zhang, Y., and Wu, X.: Distal mud deposits associated with the Pearl River over the northwestern continental shelf of the South China Sea, *Marine Geology*, 347, 43-57, 10.1016/j.margeo.2013.10.012, 2014.

Liu, Z., Zhao, Y., Colin, C., Stattegger, K., Wiesner, M. G., Huh, C.-A., Zhang, Y., Li, X., Sompongchaiyakul, P., You, C.-F., Huang, C.-Y., Liu, J. T., Siringan, F. P., Le, K. P., Sathiamurthy, E., Hantoro, W. S., Liu, J., Tuo, S., Zhao, S., Zhou, S., He, Z., Wang, Y., Bunsomboonsakul, S., and Li, Y.: Source-to-sink transport processes of fluvial sediments in the South China Sea, *Earth-Science Reviews*, 153, 238-273, 10.1016/j.earscirev.2015.08.005, 2016.

Lu, X., Wang, Z., Guo, X., Gu, Y., Liang, W., and Liu, L.: Impacts of metal contamination and eutrophication on dinoflagellate cyst assemblages along the Guangdong coast of southern China, *Marine Pollution Bulletin*, 120, 239-249, 10.1016/j.marpolbul.2017.05.032, 2017.

Ma, C., Zhao, J., Ai, B., Sun, S., and Yang, Z.: Machine Learning Based Long-Term Water Quality in the Turbid Pearl River Estuary, China, *Journal of Geophysical Research: Oceans*, 127, 10.1029/2021jc018017, 2022.

Ma, M., Zhang, W., Chen, W., Deng, J., and Schrum, C.: Impacts of morphological change and sea-level rise on stratification in the Pearl River Estuary, *Frontiers in Marine Science*, Volume 10 - 2023, 10.3389/fmars.2023.1072080, 2023.

1436 Ma, M., Porz, L., Schrum, C., and Zhang, W.: Physical mechanisms, dynamics and interconnections of  
 1437 multiple estuarine turbidity maximum in the Pearl River estuary, *Frontiers in Marine Science*,  
 1438 Volume 11 - 2024, 10.3389/fmars.2024.1385382, 2024.

1439 Ma, Y., Friedrichs, C. T., Harris, C. K., and Wright, L. D.: Deposition by seasonal wave- and  
 1440 current-supported sediment gravity flows interacting with spatially varying bathymetry: Waiapu  
 1441 shelf, New Zealand, *Marine Geology*, 275, 199-211, <https://doi.org/10.1016/j.margeo.2010.06.001>,  
 1442 2010.

1443 Madsen, O. S.: Spectral Wave-Current Bottom Boundary Layer Flows, *Coastal Engineering* 1, 384-398,  
 1444 1994.

1445 Mao, Q., Shi, P., Yin, K., Gan, J., and Qi, Y.: Tides and tidal currents in the Pearl River Estuary,  
 1446 *Continental Shelf Research*, 24, 1797-1808, 10.1016/j.csr.2004.06.008, 2004.

1447 Marshall, J., Adcroft, A., Hill, C., Perelman, L., and Heisey, C.: A finite-volume, incompressible Navier  
 1448 Stokes model for studies of the ocean on parallel computers, *Journal of Geophysical Research:*  
 1449 *Oceans*, 102, 5753-5766, <https://doi.org/10.1029/96JC02775>, 1997a.

1450 Marshall, J., Hill, C., Perelman, L., and Adcroft, A.: Hydrostatic, quasi-hydrostatic, and nonhydrostatic  
 1451 ocean modeling, *Journal of Geophysical Research: Oceans*, 102, 5733-5752,  
 1452 <https://doi.org/10.1029/96JC02776>, 1997b.

1453 McKee, B. A., Aller, R. C., Allison, M. A., Bianchi, T. S., and Kineke, G. C.: Transport and  
 1454 transformation of dissolved and particulate materials on continental margins influenced by major  
 1455 rivers: benthic boundary layer and seabed processes, *Continental Shelf Research*, 24, 899-926,  
 1456 <https://doi.org/10.1016/j.csr.2004.02.009>, 2004.

1457 McWilliams, J. C., Restrepo, J. M., and Lane, E. M.: An asymptotic theory for the interaction of waves  
 1458 and currents in coastal waters, *Journal of Fluid Mechanics*, 511, 135-178,  
 1459 10.1017/s0022112004009358, 2004.

1460 Meade, R. H.: Landward Transport of Bottom Sediments in Estuaries of the Atlantic Coastal Plain,  
 1461 *Journal of Sedimentary Petrology*, 39, 222-234, 1969.

1462 Milliman, J., and Farnsworth, K. L.: River discharge to the coastal ocean: A global synthesis. UK:  
 1463 Cambridge University Press; ISBN 978-0-521-87987-3, 2011.

1464 Moriarty, J. M., Harris, C. K., Friedrichs, M. A. M., Fennel, K., and Xu, K.: Impact of Seabed

1465 Resuspension on Oxygen and Nitrogen Dynamics in the Northern Gulf of Mexico: A Numerical  
 1466 Modeling Study, *Journal of Geophysical Research: Oceans*, 123, 7237-7263,  
 1467 <https://doi.org/10.1029/2018JC013950>, 2018.  
 1468 Nan, F., Xue, H., and Yu, F.: Kuroshio intrusion into the South China Sea: A review, *Progress in*  
 1469 *Oceanography*, 137, 314-333, <https://doi.org/10.1016/j.pocean.2014.05.012>, 2015.  
 1470 Ning, L., and Qian, Y.: Interdecadal change in extreme precipitation over South China and its  
 1471 mechanism, *Advances in Atmospheric Sciences*, 26, 109-118, 10.1007/s00376-009-0109-x, 2009.  
 1472 Nittrouer, C. A., and Wright, L. D.: Transport of particles across continental shelves, *Reviews of*  
 1473 *Geophysics*, 32, 85-113, <https://doi.org/10.1029/93RG02603>, 1994.  
 1474 Orlanski, I.: A simple boundary condition for unbounded hyperbolic flows, *Journal of Computational*  
 1475 *Physics*, 21, 251-269, 10.1016/0021-9991(76)90023-1, 1976.  
 1476 Ou, S., Zhang, H., and Wang, D.: Dynamics of the buoyant plume off the Pearl River Estuary in  
 1477 summer, *Environmental Fluid Mechanics*, 9, 471-492, 10.1007/s10652-009-9146-3, 2009.  
 1478 Ralston, D. K., Geyer, W. R., and Warner, J. C.: Bathymetric controls on sediment transport in the  
 1479 Hudson River estuary: Lateral asymmetry and frontal trapping, *Journal of Geophysical Research:*  
 1480 *Oceans*, 117, 10.1029/2012jc008124, 2012.  
 1481 Ralston, D. K., and Geyer, W. R.: Sediment Transport Time Scales and Trapping Efficiency in a Tidal  
 1482 River, *Journal of Geophysical Research: Earth Surface*, 122, 2042-2063, 10.1002/2017jf004337,  
 1483 2017.  
 1484 Raymond, W. H., and Kuo, H. L.: A radiation boundary condition for multi-dimensional flows,  
 1485 *Quarterly Journal of the Royal Meteorological Society*, 110, 535-551, 1984.  
 1486 Repasch, M., Scheingross, J. S., Hovius, N., Lupker, M., Wittmann, H., Haghipour, N., Gröcke, D. R.,  
 1487 Orfeo, O., Eglinton, T. I., and Sachse, D.: Fluvial organic carbon cycling regulated by sediment  
 1488 transit time and mineral protection, *Nature Geoscience*, 14, 842-848,  
 1489 10.1038/s41561-021-00845-7, 2021.  
 1490 Saha, S., Moorthi, S., Wu, X., Wang, J., Nadiga, S., Tripp, P., Behringer, D., Hou, Y.-T., Chuang, H.-y.,  
 1491 Iredell, M., Ek, M., Meng, J., Yang, R., Mendez, M. P., van den Dool, H., Zhang, Q., Wang, W.,  
 1492 Chen, M., and Becker, E.: The NCEP Climate Forecast System Version 2, *Journal of Climate*, 27,  
 1493 2185-2208, <https://doi.org/10.1175/JCLI-D-12-00823.1>, 2014.

1494 Sanford, L. P.: Wave-forced resuspension of upper Chesapeake Bay muds, *Estuaries*, 17, 148-165,  
 1495 1994.

1496 Shchepetkin, A. F., and McWilliams, J. C.: The regional oceanic modeling system (ROMS): a  
 1497 split-explicit, free-surface, topography-following-coordinate oceanic model, *Ocean Modelling*, 9,  
 1498 347-404, <https://doi.org/10.1016/j.ocemod.2004.08.002>, 2005.

1499 Shepard, F. P.: Nomenclature Based on Sand-silt-clay Ratios, *Journal of Sedimentary Research*, 24,  
 1500 151-158, 1954.

1501 Sherwood, C. R., Aretxabaleta, A. L., Harris, C. K., Rinehimer, J. P., Verney, R., and Ferré, B.:  
 1502 Cohesive and mixed sediment in the Regional Ocean Modeling System (ROMS v3.6)  
 1503 implemented in the Coupled Ocean–Atmosphere–Wave–Sediment Transport Modeling System  
 1504 (COAWST r1234), *Geoscientific Model Development*, 11, 1849-1871,  
 1505 10.5194/gmd-11-1849-2018, 2018.

1506 Shi, M., Chen, C., Xu, Q., Lin, H., Liu, G., Wang, H., Wang, F., and Yan, J.: The Role of Qiongzhou  
 1507 Strait in the Seasonal Variation of the South China Sea Circulation, *Journal of Physical*  
 1508 *Oceanography*, 32, 103-121, 2002.

1509 Skamarock, W. C., Klemp, J. B., Dudhia, J., Gill, D. O., Barker, D. M., Wang, W., and Powers, J. G.: A  
 1510 Description of the Advanced Research WRF Version 2, 2005,

1511 Smagorinsky, J.: GENERAL CIRCULATION EXPERIMENTS WITH THE PRIMITIVE  
 1512 EQUATIONS, *Monthly Weather Review*, 91, 99-164,  
 1513 10.1175/1520-0493(1963)091<0099:gcewtp>2.3.co;2, 1963.

1514 Song, Y., and Haidvogel, D.: A Semi-implicit Ocean Circulation Model Using a Generalized  
 1515 Topography-Following Coordinate System, *Journal of Computational Physics*, 115, 228-244,  
 1516 <https://doi.org/10.1006/jcph.1994.1189>, 1994.

1517 Ståhlberg, C., Bastviken, D., Svensson, B. H., and Rahm, L.: Mineralisation of organic matter in  
 1518 coastal sediments at different frequency and duration of resuspension, *Estuarine, Coastal and Shelf*  
 1519 *Science*, 70, 317-325, <https://doi.org/10.1016/j.ecss.2006.06.022>, 2006.

1520 Su, J.: Overview of the South China Sea circulation and its influence on the coastal physical  
 1521 oceanography outside the Pearl River Estuary, *Continental Shelf Research*, 24, 1745-1760,  
 1522 10.1016/j.csr.2004.06.005, 2004.



- 1523 Sun, Z., Zhang, Z., Qiu, B., Zhang, X., Zhou, C., Huang, X., Zhao, W., and Tian, J.: Three-Dimensional  
1524 Structure and Interannual Variability of the Kuroshio Loop Current in the Northeastern South  
1525 China Sea, *Journal of Physical Oceanography*, 50, 2437-2455,  
1526 <https://doi.org/10.1175/JPO-D-20-0058.1>, 2020.
- 1527 Tolman, H., Accensi, M., Alves, J.-H., Ardhuin, F., Barbariol, F., Benetazzo, A., Bennis, A.-C., Bidlot,  
1528 J., Booij, N., Boutin, G., Campbell, T., Chalikov, D., Chawla, A., Cheng, S., Collins Iii, C., Filipot,  
1529 J.-F., Foreman, M., Janssen, P., Leckler, F., and Westhuysen, A.: User manual and system  
1530 documentation of WAVEWATCH III (R) version 5.16, 2016.
- 1531 Turner, A., and Millward, G. E.: Suspended Particles: Their Role in Estuarine Biogeochemical Cycles,  
1532 *Estuarine, Coastal and Shelf Science*, 55, 857-883, 10.1006/ecss.2002.1033, 2002.
- 1533 van der Wegen, M., Dastgheib, A., Jaffe, B. E., and Roelvink, D.: Bed composition generation for  
1534 morphodynamic modeling: case study of San Pablo Bay in California, USA, *Ocean Dynamics*, 61,  
1535 173-186, 10.1007/s10236-010-0314-2, 2010.
- 1536 Walsh, J. P., and Nittrouer, C. A.: Understanding fine-grained river-sediment dispersal on continental  
1537 margins, *Marine Geology*, 263, 34-45, 10.1016/j.margeo.2009.03.016, 2009.
- 1538 Wang, C., Li, W., Chen, S., Li, D., Wang, D., and Liu, J.: The spatial and temporal variation of total  
1539 suspended solid concentration in Pearl River Estuary during 1987-2015 based on remote sensing,  
1540 *Science of The Total Environment*, 618, 1125-1138, 10.1016/j.scitotenv.2017.09.196, 2018.
- 1541 Wang, C., Liu, Z., Harris, C. K., Wu, X., Wang, H., Bian, C., Bi, N., Duan, H., and Xu, J.: The Impact  
1542 of Winter Storms on Sediment Transport Through a Narrow Strait, Bohai, China, *Journal of*  
1543 *Geophysical Research: Oceans*, 125, e2020JC016069, <https://doi.org/10.1029/2020JC016069>,  
1544 2020.
- 1545 Wang, S., Zhang, N., Chen, H., Li, L., and Yan, W.: The surface sediment types and their rare earth  
1546 element characteristics from the continental shelf of the northern south China sea, *Continental*  
1547 *Shelf Research*, 88, 185-202, 10.1016/j.csr.2014.08.005, 2014.
- 1548 Wang, S., Wu, S., Yan, W., Huang, W., Miao, L., Lu, J., Chen, Z., and Liu, F.: Rare metal elements in  
1549 surface sediment from five bays on the northeastern coast of the South China Sea, *Environmental*  
1550 *Earth Sciences*, 74, 4961-4971, 10.1007/s12665-015-4504-6, 2015.
- 1551 Wang, S., Li, J., Wu, S., Yan, W., Huang, W., Miao, L., and Chen, Z.: The distribution characteristics of

1552 rare metal elements in surface sediments from four coastal bays on the northwestern South China  
1553 Sea, *Estuarine, Coastal and Shelf Science*, 169, 106-118, 10.1016/j.ecss.2015.12.001, 2016.

1554 Wang, Y., Wang, Y., Wan, X., Huang, C., Wang, R., Liu, X., Yi, J., and Zhang, Y.: Influence of the  
1555 Hanjiang River's Inlet Sediment Decrease on Modern Sedimentation in the Underwater Delta,  
1556 *Applied Sciences*, 13, 8039, 10.3390/app13148039, 2023.

1557 Warner, J. C., Sherwood, C. R., Arango, H. G., and Signell, R. P.: Performance of four turbulence  
1558 closure models implemented using a generic length scale method, *Ocean Modelling*, 8, 81-113,  
1559 10.1016/j.ocemod.2003.12.003, 2005.

1560 Warner, J. C., Sherwood, C. R., Signell, R. P., Harris, C. K., and Arango, H. G.: Development of a  
1561 three-dimensional, regional, coupled wave, current, and sediment-transport model, *Computers &*  
1562 *Geosciences*, 34, 1284-1306, 10.1016/j.cageo.2008.02.012, 2008.

1563 Warner, J. C., Armstrong, B., He, R., and Zambon, J. B.: Development of a Coupled  
1564 Ocean–Atmosphere–Wave–Sediment Transport (COAWST) Modeling System, *Ocean Modelling*,  
1565 35, 230-244, 10.1016/j.ocemod.2010.07.010, 2010.

1566 Warner, J. C., Schwab, W. C., List, J. H., Safak, I., Liste, M., and Baldwin, W.: Inner-shelf ocean  
1567 dynamics and seafloor morphologic changes during Hurricane Sandy, *Continental Shelf Research*,  
1568 138, 1-18, 10.1016/j.csr.2017.02.003, 2017.

1569 Weatherall, P., Marks, K. M., Jakobsson, M., Schmitt, T., Tani, S., Arndt, J. E., Rovere, M., Chayes, D.,  
1570 Ferrini, V., and Wigley, R.: A new digital bathymetric model of the world's oceans, *Earth and*  
1571 *Space Science*, 2, 331-345, <https://doi.org/10.1002/2015EA000107>, 2015.

1572 Wright, L. D., and Coleman, J. M.: Variations in Morphology of Major River Deltas as Functions of  
1573 Ocean Wave and River Discharge Regimes, *AAPG Bulletin*, 57, 370-398, 1973.

1574 Wright, L. D., and Nittrouer, C. A.: Dispersal of river sediments in coastal seas: Six contrasting cases,  
1575 *Estuaries*, 18, 494-508, 10.2307/1352367, 1995.

1576 Wu, C., Xing, W., Jie, R., Yun, B., Zhigang, H., Yiaping, L., Heyin, S., and Wenyan, Z.:  
1577 Morphodynamics of the rock-bound outlets of the Pearl River estuary, South China — A  
1578 preliminary study, *Journal of Marine Systems*, 82, S17-S27, 10.1016/j.jmarsys.2010.02.002, 2010.

1579 Wu, Z., Milliman, J. D., Zhao, D., Zhou, J., and Yao, C.: Recent geomorphic change in LingDing Bay,  
1580 China, in response to economic and urban growth on the Pearl River Delta, Southern China,

1581 Global and Planetary Change, 123, 1-12, 10.1016/j.gloplacha.2014.10.009, 2014.

1582 Wu, Z., Milliman, J. D., Zhao, D., Cao, Z., Zhou, J., and Zhou, C.: Geomorphologic changes in the  
 1583 lower Pearl River Delta, 1850–2015, largely due to human activity, *Geomorphology*, 314, 42-54,  
 1584 10.1016/j.geomorph.2018.05.001, 2018.

1585 Wu, Z. Y., Saito, Y., Zhao, D. N., Zhou, J. Q., Cao, Z. Y., Li, S. J., Shang, J. H., and Liang, Y. Y.:  
 1586 Impact of human activities on subaqueous topographic change in Lingding Bay of the Pearl River  
 1587 estuary, China, during 1955-2013, *Scientific Reports*, 6, 37742, 10.1038/srep37742, 2016.

1588 Xia, X. M., Li, Y., Yang, H., Wu, C. Y., Sing, T. H., and Pong, H. K.: Observations on the size and  
 1589 settling velocity distributions of suspended sediment in the Pearl River Estuary, China,  
 1590 *Continental Shelf Research*, 24, 1809-1826, 10.1016/j.csr.2004.06.009, 2004.

1591 Xu, K., Corbett, D. R., Walsh, J. P., Young, D., Briggs, K. B., Cartwright, G. M., Friedrichs, C. T.,  
 1592 Harris, C. K., Mickey, R. C., and Mitra, S.: Seabed erodibility variations on the Louisiana  
 1593 continental shelf before and after the 2011 Mississippi River flood, *Estuarine, Coastal and Shelf  
 1594 Science*, 149, 283-293, <https://doi.org/10.1016/j.ecss.2014.09.002>, 2014.

1595 Xu, K., Mickey, R. C., Chen, Q., Harris, C. K., Hetland, R. D., Hu, K., and Wang, J.: Shelf sediment  
 1596 transport during hurricanes Katrina and Rita, *Computers & Geosciences*, 90, 24-39,  
 1597 <https://doi.org/10.1016/j.cageo.2015.10.009>, 2016.

1598 Xue, Z., He, R., Liu, J. P., and Warner, J. C.: Modeling transport and deposition of the Mekong River  
 1599 sediment, *Continental Shelf Research*, 37, 66-78, 10.1016/j.csr.2012.02.010, 2012.

1600 Yang, B., Liu, S.-M., and Zhang, G.-L.: Geochemical characteristics of phosphorus in surface  
 1601 sediments from the continental shelf region of the northern South China Sea, *Marine Chemistry*,  
 1602 198, 44-55, 10.1016/j.marchem.2017.11.001, 2018.

1603 Yang, J., Wu, D., and Lin, X.: On the dynamics of the South China Sea Warm Current, *Journal of  
 1604 Geophysical Research: Oceans*, 113, <https://doi.org/10.1029/2007JC004427>, 2008.

1605 Young, I. R., Zieger, S., and Babanin, A. V.: Global trends in wind speed and wave height, *Science*, 332,  
 1606 451-455, 10.1126/science.1197219, 2011.

1607 Zang, Z., Xue, Z. G., Xu, K., Bentley, S. J., Chen, Q., D'Sa, E. J., and Ge, Q.: A Two Decadal  
 1608 (1993–2012) Numerical Assessment of Sediment Dynamics in the Northern Gulf of Mexico,  
 1609 *Water*, 11, 938, 2019.

1610 Zeng, X., He, R., Xue, Z., Wang, H., Wang, Y., Yao, Z., Guan, W., and Warrillow, J.: River-derived  
 1611 sediment suspension and transport in the Bohai, Yellow, and East China Seas: A preliminary  
 1612 modeling study, *Continental Shelf Research*, 111, 112-125,  
 1613 <https://doi.org/10.1016/j.csr.2015.08.015>, 2015.

1614 Zhan, W., Wu, J., Wei, X., Tang, S., and Zhan, H.: Spatio-temporal variation of the suspended sediment  
 1615 concentration in the Pearl River Estuary observed by MODIS during 2003–2015, *Continental*  
 1616 *Shelf Research*, 172, 22-32, 10.1016/j.csr.2018.11.007, 2019.

1617 Zhang, G., Cheng, W., Chen, L., Zhang, H., and Gong, W.: Transport of riverine sediment from  
 1618 different outlets in the Pearl River Estuary during the wet season, *Marine Geology*, 415, 105957,  
 1619 10.1016/j.margeo.2019.06.002, 2019.

1620 Zhang, G., Chen, Y., Cheng, W., Zhang, H., and Gong, W.: Wave Effects on Sediment Transport and  
 1621 Entrapment in a Channel-Shoal Estuary: The Pearl River Estuary in the Dry Winter Season,  
 1622 *Journal of Geophysical Research: Oceans*, 126, 10.1029/2020jc016905, 2021.

1623 Zhang, G., Hu, P., Hu, S., Zhang, H., and Gong, W.: Tidal effects on the dispersal and water age of the  
 1624 plumes from eight outlets of the Pearl river during the wet summer, *Ocean & Coastal Management*,  
 1625 266, 107704, <https://doi.org/10.1016/j.ocecoaman.2025.107704>, 2025.

1626 Zhang, J., Jiang, Q., Jeng, D., Zhang, C., Chen, X., and Wang, L.: Experimental Study on Mechanism  
 1627 of Wave-Induced Liquefaction of Sand-Clay Seabed, *Journal of Marine Science and Engineering*,  
 1628 8, 66, 10.3390/jmse8020066, 2020.

1629 Zhang, W., Wei, X., Zheng, J., Zhu, Y., and Zhang, Y.: Estimating suspended sediment loads in the  
 1630 Pearl River Delta region using sediment rating curves, *Continental Shelf Research*, 38, 35-46,  
 1631 10.1016/j.csr.2012.02.017, 2012.

1632 Zhang, W., Zheng, J., Ji, X., Hoitink, A. J. F., van der Vegt, M., and Zhu, Y.: Surficial sediment  
 1633 distribution and the associated net sediment transport pattern retain-->in the Pearl River Estuary,  
 1634 South China, *Continental Shelf Research*, 61-62, 41-51, 10.1016/j.csr.2013.04.011, 2013.

1635 Zhang, Y. J., Ye, F., Stanev, E. V., and Grashorn, S.: Seamless cross-scale modeling with SCHISM,  
 1636 *Ocean Modelling*, 102, 64-81, <https://doi.org/10.1016/j.ocemod.2016.05.002>, 2016.

1637 Zhong, Y., Chen, Z., Li, L., Liu, J., Li, G., Zheng, X., Wang, S., and Mo, A.: Bottom water  
 1638 hydrodynamic provinces and transport patterns of the northern South China Sea: Evidence from

1639 grain size of the terrigenous sediments, *Continental Shelf Research*, 140, 11-26,  
1640 10.1016/j.csr.2017.01.023, 2017.

1641 Zong, X., Cheng, X., Zhang, S., Lian, Q., Deng, F., and Chen, Z.: Tidal effects on dynamics and  
1642 freshwater transport of a medium-scale river plume with multiple outlets, *Ocean Modelling*, 188,  
1643 102338, <https://doi.org/10.1016/j.ocemod.2024.102338>, 2024.

1644 Zong, Y., Huang, K., Switzer, A., yu, F., and Yim, W.: An evolutionary model for the Holocene  
1645 formation of the Pearl River delta, China, *The Holocene*, 19, 129-142,  
1646 10.1177/0959683608098957, 2009.

1647